THEORETICAL INVESTIGATION OF LASER PRODUCED Ni-LIKE Sn PLASMA

A THESIS SUBMITED TO
THE GRADUATE SCHOOL OF NATURAL AND APPLIED SCIENCES
OF
MIDDLE EAST TECHNICAL UNIVERSITY

BY

ELİF YURDANUR

IN PARTIAL FULFILLMENT OF THE REQUIREMENTS
FOR
THE DEGREE OF MASTER OF SCIENCE
IN
PHYSICS

SEPTEMBER 2006

Approval of the Graduate School of Natural and Applied Sciences.

Prof. Dr. Canan Özgen
Director

I certifty that this thesis satisfies all the requirements as a thesis for the degree of Master of Science.

Prof. Dr. Sinan Bilikmen
Head of Department

This is to certify that we have read this thesis and that in our opinion it is fully adequate, in scope and quality, as a thesis for degree of Master of Science.

Prof. Dr. Sinan Bilikmen
Supervisor

Examining Committee Members

Prof. Dr. Arif Demir	(KOU, PHYS)	
Prof. Dr. Sinan Bilikmen	(METU, PHYS)	
Prof. Dr. Gülay Öke	(METU, PHYS)	
Assist. Prof. İsmail Rafatov	(METU, PHYS)	
Dr. Burak Yedierler	(METU, PHYS)	

I hereby declare that all information in this document has been obtained and presented in accordance with academic rules and ethical conduct. I also declare that, as required by these rules and conduct, I have fully cited and referenced all material and results that are not original to this work.

Name, Last name: Elif Yurdanur

Signature :

ABSTRACT

THEORETICAL INVESTIGATION OF LASER PRODUCED Ni-LIKE Sn PLASMA

YURDANUR, ELİF
M.S., Department of Physics
Supervisor: Prof. Dr. Sinan Bilikmen

September 2006, 77 pages

In this thesis, theoretical investigation of nickel-like tin plasma is presented. X-ray production in a plasma medium produced by a laser beam is reviewed. Applications mostly, lithography are discussed. Two different schemes for x-ray lasing, namely, quasi-steady state and transient collisional excitation are explained and compared. The computer codes that are used for plasma, especially for laser produced plasma and x-ray laser including hydrodynamic codes, ray-trace codes and collisional radiative codes are discussed. The code used in this work, EHYBRID, is considered in more detail. An experimental setup which can allow x-ray lasing is designed for different plasma and laser parameters are analyzed by means of EHYBRID code. Results are briefly discussed and as a future work the realization of the related experiment is mentioned.

Keywords: X-ray laser, lithography, hydrodynamic code: EHYBRID, quasisteady state (QSS), transient collisional excitation (TCE)

ÖZ

LAZERLE ÜRETİLEN Ni-BENZERİ Sn PLAZMANIN TEORİK İNCELENMESİ

YURDANUR, ELİF
Yüksek Lisans, Fizik Bölümü
Tez Yöneticisi: Prof. Dr. Sinan Bilikmen

Eylül 2006, 77 Sayfa

Bu tezde, nikel benzeri kalay plazmasının teorik olarak incelenmesi sunulmaktadır.Lazer ile oluşturulmuş plazma ortamındaki x-ışını üretimi gözden geçirilmiştir. Uygulama alanları özellikle de litografi ele alınmıştır. İki farklı şema olan yarı-kararlı ile geçici çarpışmalı uyarılma durumları açıklanmış ve karşılaştırılmıştır. Plazma için, özellikle de lazerle oluşturulan plazma ve x-ışını için kullanılan kodlarından hidrodinamik, ışın izi kodu ve çarpışmalı ışıma kodları başta olmak üzere bilgisayar kodları incelenmiştir. bu çalışmada kullanılan kod olan EHYBRID daha fazla detaylandırılarak anlatılmıştır. X-ışını lazeri yapmaya olanak sağlayan bir deneysel düzenek saptanmış ve farklı plazma ve lazer parametreleri EHYBRID kodu ile analiz edilmiştir. Sonuçlar değerlendirilmiş ve sözü geçen deneyin hayata kavuşturulmasına değinilmiştir.

Anahtar Sözcükler: X-ışını lazeri, litografi, hidrodinamik kod: EHYBRID, yarı-kararlı durum (QSS), geçici çarpışmalı uyarılma (TCE)

To My Parents

ACKNOWLEDGEMENTS

I wish to express my deepest gratitude to my supervisor Prof. Dr. Sinan Bilikmen for his guidance, support and encouragements throughout the work.

I would also like to thank Prof. Dr. Arif Demir, Assist. Prof. Dr. Elif Kaçar for their helpful discussions and comments.

My special thanks go to Dr. Burak Yedierler for his kind support, criticism and advice on the thesis, laser laboratory members especially Mr. Salur Kurucu for the great efforts, my office mates Ms. Sevi İnce and Mr. Mustafa Huş for their friendly supports and to Mr. Emre Taşçı for technical assistance.

I especially thank my mother, Ayla Yurdanur and father, Önder Yurdanur for their patience all through this work, sensibility and endless love.

Last but not least, I would like to thank to Erdinç Taşel, my love, for his endless patience and love.

TABLE OF CONTENTS

LIST OF TABLES

LIST OF FIGURES

FIGURES

LIST OF SYMBOLS AND ABBREVIATIONS

ε_0	:Dielectric Constant
μJ	:Microjoule (10^{-6}J)
1D	:One Dimensional
Ar	:Argon
ASE	:Amplified Spontaneous Emission
ATI	:Above-threshold-ionization
B_{12}	:Einstein Coefficient for Absorption
B_{21}	:Einstein Coefficient for Stimulated Emission
c	:Speed of Light
CCD	:Charged-Coupled Device
CE	:Conversion Efficiency
Co	:Cobalt
CPA	:Chirped Pulse Amplification
CRM	:Collisional Radiative Model
DPP	:Discharge Produced Plasma
E	:Electric Field
e	:Electron Charge
EUV	:Extreme Ultra-violet
EUVL	:Extreme Ultra-violet Lithography
eV	:Electron Volt
FEL	:Free Electron Laser
fs	:Femtosecond (10^{-15}s)
FWHM	:Full Width Half Maximum
Gd	:Gadolinium
Ge	:Germanium
He	:Helium
J	:Joule
keV	:Kiloelectron Volt
KOU	:Kocaeli University
LLNL	:Lawrence Livermore National Laboratory
LLP	:Laser Produced Plasma
MCDF	:Multiconfigurational Dirac-Fock
m_e	:Electron Mass
METU	:Middle East Technical University
mJ	:Millijoule
Mo	:Molybdenum
N	:Refractive Index
n_c	:Critical Density
Nd	:Neodymium
Ne	:Neon

n_e	:Plasma Electron Density
Ni	:Nickel
nm	:Nanometer (10^{-9}m)
OFI	:Optical Field Ionization
ps	:Picosecond (10^{-12}s)
QSS	:Quasisteady State
Si	:Silicon
Sn	:Tin
TCE	:Transient Collisional Excitation
T_e	:Electron Temperature
W	:Watt
w	:Frequency of the Heating Laser
w_p	:Plasma Frequency
XUV	:Extreme Ultra-violet
YAG	:Yttrium Aluminum Garnet
Z	:Atomic Weight

CHAPTER 1

INTRODUCTION

It is never possible to predict when a development in technology will fire the imagination of the scientific community. Many years ago, it was the transistor, which stimulated a worldwide flowering of physics. After that, invention of laser brought the various systems to the state of the art, one of which is the x-ray lasers.

In this thesis, x-ray emission mostly from tin target which is a strong candidate for x-ray lasing and lithography is studied. X-ray lasers have many application and research area that is why many research groups studies x-ray transitions and lasing at that region for about thirty years.

In Chapter 2, x-ray laser attempts from 1980s till now is summarized and a systematic development for x-ray lasing is discussed. X-ray formation, the preferable way to produce laser including plasma media and laser produced plasma media are briefly reviewed. Applications on x-ray laser is summarized and lithography among them is stressed since tin is one of the few candidates for it. Two different schemes for x-ray lasing, namely, quasi-steady state and transient excitation are explained and some comparison from the literature is presented.

In chapter 3, importance of simulation is mentioned. After that, the computer codes that are used for plasma, especially for laser produced plasma and x-ray laser including hydrodynamic codes, ray-trace codes and collisional radiative codes are taken into account. Then the code used during this study, EHYBRID, is discussed in detail and the reliability of the code is shown with examples.

In Chapter 4, an experimental setup which can allow x-ray lasing is proposed. Nickel like tin resonance lines are calculated and compared with real lines. Different plasma and laser parameters including full width at half maximum, ionization degree, gain, electron temperature and density are analyzed by the means of graphs from EHYBRID code and compared for altering spot size and intensity of the pumping laser pulse. The contrasts between quasi-steady state and transient excitation schemes are discussed and the former is verified by experiments from literature.

In Chapter 5, a brief summary of the thesis is given with concluding inferences. Next, a future work and proposals are mentioned.

CHAPTER 2

BACKGROUND OF X-RAY LASERS

X-ray regime and lasing are interesting and have challenging topics. Many research groups discussed this regime and have performed experiments on it. Different attempts and simulations improve the x-ray investigation together with x-ray lasing.

2.1. Progresses on X-Ray Lasers

Measurement of definitive high output lasing at wavelengths shorter than the ultra-violet was illogical except for some theoretical studies until the mid 1980s when conclusive evidence for an 'x-ray laser' [1], [2].

There are now, several schemes for producing x-ray lasing; using a capillary discharge, a free-electron laser, optical field ionization of a gas cell, laser produced plasma-based recombination lasers and laser produced plasma-based collisional x-ray lasers. Capillary discharges, free-electron lasers and optical field ionization have not yet produced laser action at wavelengths shorter than 47 nm, 50 nm and 32.8 nm, respectively, but can potentially do so [3]. Recombination lasers have produced significant output at typically 18 nm, but saturation has not been observed [3]. Regarding their evolution since 1980s, laser produced plasma-based collisional x-ray lasers are the most suitable candidates for x-ray lasers.

J.J. Rocca et al. reported the first demonstration of a large soft x-ray amplifier at 46.9 nm on the 3p-3s J=0→1 transition in Ne-like Ar plasma by capillary discharge in 1994 [4]. Four years later, Moreno et al. [5] brought about two-dimensional near-field and far-field measurements over a wide range of discharge

parameters, although the experimental and modeling results were in a good agreement it is not so common for x-ray application due to the long wavelength.

One of the desired next-generation light source is high-gain, single-pass free-electron laser (FEL) [6], which is still not lasing in a short wavelength, but at 51.7 nm as the fundamental radiation value.

First, Chou et al. [7], demonstrated an optical-field-ionization (OFI) soft x-ray laser with prepulse-controlled nanoplasma expansion in a cluster gas jet. Pd-like xenon lasing at 41.8 nm with 95 nJ pulse energy was achieved, indicating near-saturation amplification. Strong amplification at 32.8 nm of Ni-like krypton was later demonstrated, with a 760-mJ, 30-fs, circularly polarized laser pulse [8]. A schematic view for formation of OFI is given in Figure 1.

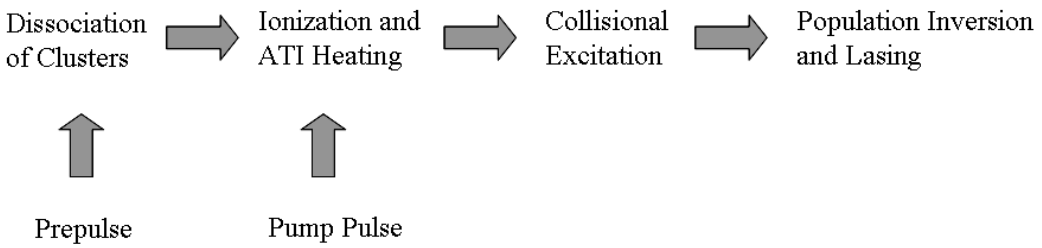

Figure 1 Schematic formation of OFI x-ray laser with clustered gas jet, ATI refers to above-threshold-ionization [9]

In the calculation by Zhang et al. [10], recombination x-ray laser seems to lase at 4.55 nm using ultrashort pulse drivers. However, their calculation did not include the effects caused by non-uniform irradiation along the plasma. Besides, as one of the authors of this study, mentioned in a different journal that this is not convenient with experimental results, the shortest wavelength for recombination laser is still about 20 nm and without dealing with saturation [3].

The first laser produced plasma-based collisional x-ray lasers were produced using thin foil targets with complete ablation of the foils [1]. It was soon found,

however, that irradiation of thick slab targets with ablation of a thin layer of the target could produce lasing with relatively modest facilities. Saturated x-ray laser output was observed for the first time with slab targets [11]. The next advance was to use a pre-pulse to create a pre-plasma into which the main optical pumping pulse was incident [12]. Using prepulse increased the efficiency of the x-ray lasers. And also the output has improved by utilizing some high reflectivity mirrors [12]. Pumping laser pulses of duration down to the picosecond have now been used to irradiate pre-plasmas created with prepulses with resultant short duration of gain and output lasing duration [13], [14]. Recent works have shown that it is possible to have saturated x-ray lasing pumped with near table-top sized picosecond duration optical lasers [15] producing only a few joules of output. Scaling to shorter wavelength operation has been achieved through the use of higher Z targets [16] allowing the efficient operation of Ni-like rather than Ne-like ion x-ray lasers, with the uses of pre-formed plasmas and curved targets [3].

Matthews et al. [1], reported the first observations of amplified spontaneous emission at soft x-ray wavelengths in 1985. This x-ray was created in plasma produced by focusing the most energetic nanosecond duration infrared laser available for 1985, NOVA at Lawrence Livermore National Laboratory, into a line on a foil target. In the neon-like collisional excitation scheme, the transition was $2p^5 3p \rightarrow 2p^5 3s$ for selenium. In their experiment, they used many spectroscopic instruments to measure the time-resolved absolute brightness of the amplified spontaneous emission (Section 2.1.2), and to demonstrate the nonlinear increase of the emission. A 75 nm layer of Se-thin foil target was illuminated by 532 nm green laser along a line of focus. In the experimental spectra, the 20.63 nm and 20.96 nm lines are strong that showed population inversion and ASE at soft x-ray region.

Deploying the three beams, from six-beam Vulcan Nd: Glass was incident to Ge slab target in the work of Carillion et al. [11], produced 22-mm line focus. Using slab target together with the Mo: Si multilayer high reflectivity mirrors, laser output at 23.6 nm was increased by a factor of 30.

Nilsen et al. [12] performed x-ray laser experiments at the University of Bern with a 1054-nm Nd:glass laser. This laser was capable of delivering 40 J at a pulse duration of 100 ps (FWHM). The target was a 2.5-cm-long diamond-machined Sn slab. In order to obtain defined prepulses at variable delays, different beam splitters were inserted into an optical delay line in the double-passed final amplifier stage. For the Sn x-ray laser imaging experiments a 0.5% prepulse was used; it preceded the main laser pulse by 6 ns. The prepulse heats the target and enables the main pulse irradiate more sufficiently. The schematic experimental setup showing the pump beam illuminating the 2.5-cm-long Sn slab target can be seen in Figure 2. The output aperture of the 11.9-nm Ni-like Sn x-ray laser line is imaged with a magnification of 10 onto the P43 phosphor and CCD camera detection system.

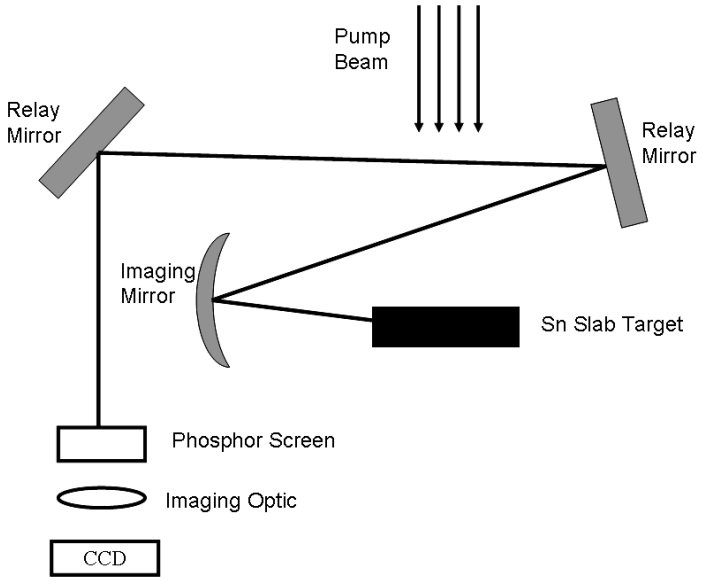

Figure 2 Schematic experimental setup [11]

In this work, Nilsen et al. [12] also utilized multilayer mirrors made of altering layers of Mo and Y that produce high reflectivity at the normal incidence. After usage of the Mo: Si mirrors [13], [11] which have reflectivity as high as 70% at normal incidence but work well only at wavelengths longer than 12.5 nm because

of the Si L-shell absorption edge; using Mo:Y multilayer was a development for 11.9 nm x-ray together with the prepulse technique.

Smith et al. [13] presented the first results from picosecond interferometry of dense laser-produced plasmas using a soft x-ray laser. The Ni-like Pd 14.7 nm x-ray laser probe beam and the plasma to be studied were generated using three laser beams at 1054 nm wavelength from the COMET facility at Lawrence Livermore National Laboratory. The single pass saturated x-ray laser output of a few tens of μJs was achieved with an optical pumping combination of a 600-ps-long pulse (2 J, $2x10^{11}$ Wcm^{-2}) and a 6ps (5 J, $7x10^{13}$ Wcm^{-2}) main heating pulse. The picosecond x-ray laser interferometry enables to diagnose large, hot, dense plasmas and triggered improvement.

After chirped pulse amplification (CPA), in which a short pulse is stretched to form a rather long pulse, then long pulse is amplified and compressed back to its original short circumstance, come to the stage, the output laser durations decreased. In the journal of Tallents et al. [14], it is shown that short duration (picosecond) pumping can produce x-ray laser pulses of a few picosecond duration and that measurement of the emission from the plasma can give an estimate of the duration of the gain coefficient. In the experiment, x-ray lasing was produced in Ni-like silver at 13.9 nm and Ne-like nickel at 23.1 nm by irradiating solid silver or nickel slabs with two beams of wavelength 1064 nm from the VULCAN glass laser at the Rutherford Appleton Laboratory. For Ne-like nickel, a preplasma was formed with a background pulse of duration 280 ps and peak irradiance $2x10^{13}$ Wcm^{-2} in a line focus of length 16 mm and width 100 μm. The main pulse irradiance is enhanced by chirp pulse amplification (CPA) to give duration of 1.2 ps and peak irradiance $7x10^{15}$ Wcm^{-2} in a line focus of length 12mm and width 100 μm.

Through the use of CPA technique, pump energy requirement is reduced. The reduction from ~250 J to ~60 J was shown by MacPhee et al. [17] with a 280

picosecond prepulse, 550 ps before a main pulse of 3 ps of peak irradiance 10^{15} Wcm^{-2} onto a Sn coated glass slab up to 10mm.
Further reduction can be seen in the study of Kawaschi et al. [16]. Silver (Z=47) and tin (Z=50) are irradiated with CPA glass laser with pumping energies 12 J and 14 J, respectively. The laser pulses consisted of two pulses with 4ps duration, separated by 1.2 ns created a high gain 13.9 nm x-ray for Ag and 12.0 nm x-ray for Sn.

The CPA technique is implemented by adjusting into a tabletop size. The Ni-like plasma formation, ionization, and collisional excitation mostly requires irradiation of a slab target by two laser pulses. A formation beam with 5 J energy of 800 ps duration and a pump beam of 5 J energy in 1.1 ps from a table-top laser were used in the study by Dunn et al. [15]. In their letter, they reported x-ray amplification of spontaneous emission in a transient collisional excitation (Section 2.5) at 14.7 nm for Ni-like Pd with very large laser output.

2.2. X-Ray Laser Media

It has been known for many years that for short wavelength laser operations the most suitable lasing medium is plasma. X-ray photons have energies approaching 1keV, if lasing is to take place between different electronic states, then the medium should be pumped from a source at kilo-electron-volt temperatures, or else the medium at some time has to have a temperature of this order. Materials at kilo-electron-volt temperatures are in the plasma state. Furthermore, suitable electronic states, which are very energetic, have very short lifetimes of the order of 10 fs, and the power emitted by spontaneous decay from unit surface area of the plasma is very large. Since pump pulse must exceed the spontaneously emitted power, the power input per area must be very large. These reasons show that a laser-heated plasma is a very suitable medium for x-ray lasing (Key, 1985) [18]. Amplified spontaneous emission at photon energies around 50 eV in the XUV regime was first demonstrated at NOVA Laser Facility in Livermore in the USA (Matthews et al., 1985) [18]

2.2.1. Plasma

The term “plasma” was introduced by Langmuir (1982) to describe the state of matter in the positive columns of glow discharge tubes [18]. Plasma is typically an ionized gas, which primarily composed of electrons and ions which are free in a sense that their mean kinetic energy is much larger than the Coulomb potential energy.

For a matter in order to be called plasma, there are some restrictions. In plasmas, charged particles must be close enough together that each particle influences many nearby charged particles, rather than just the interacting with the closest particle (Debye length). The plasma approximation is valid when the number of electrons within the sphere of influence (the Debye sphere) of a particular particle is large. For plasma formation; this Debye length should be short enough compared to the physical size of the plasma, the electron plasma frequency should be large compared to the electron neutral collision frequency. When latter condition is valid, plasmas act to shield charges very rapidly [19] [20].

Some of the most important plasma parameters are the degree of ionization, the plasma temperature and the density. The degree of ionization of a plasma is the proportion of atoms which have lost or gained electrons, and is controlled mostly by the temperature. Plasma temperature is commonly measured in units of Kelvin or electron volts, and is roughly a measure of the thermal kinetic energy per particle. Electron and ion densities are the number of free electrons or ions per unit volume.

Although some estimates suggest that up to 99% of the entire visible universe is plasma, since it is not actually available in daily lives, it is the least investigated phase compared to the gas, liquid and solid phases. Flame and lightning are the rare examples for plasma that present on earth naturally. Besides, for investigation and applications, it can be artificially produced, one of the possible ways is to lase a material intensely.

2.2.2 Laser Produced Plasma

A high power optical laser incident onto a solid produces free electrons and ions. The root mean squared time-averaged laser electric field E is related to the laser intensity I by

$$I = \frac{1}{2}\varepsilon_0 cnE^2 \qquad (1)$$

where ε_0 is the dielectric constant, c is the speed of light in vacuum and n is the refractive index of plasma.

The electric field at the beginning of a high power laser pulse is sufficient to remove electrons from solid surface. These free electrons are then accelerated by laser electric field and produce further ionization and heating by collisions. Initially, the free electrons are accelerated. After a few hundred femtoseconds, significant numbers of ions will expand and a density profile falling approximately exponentially with distance from the solid target surface is established. Several zones of laser produced plasmas and the increase in the density profile in time are shown in Figure 3.

By absorption of the pump laser, the target surface ablates and starts to expand. The free electron density even overreaches the density of the original target material. The laser light can only penetrate up to an electron density (the 'critical density') at which the natural oscillation frequency of the electrons relative to the ions (the 'plasma frequency') equals the laser light frequency [3].

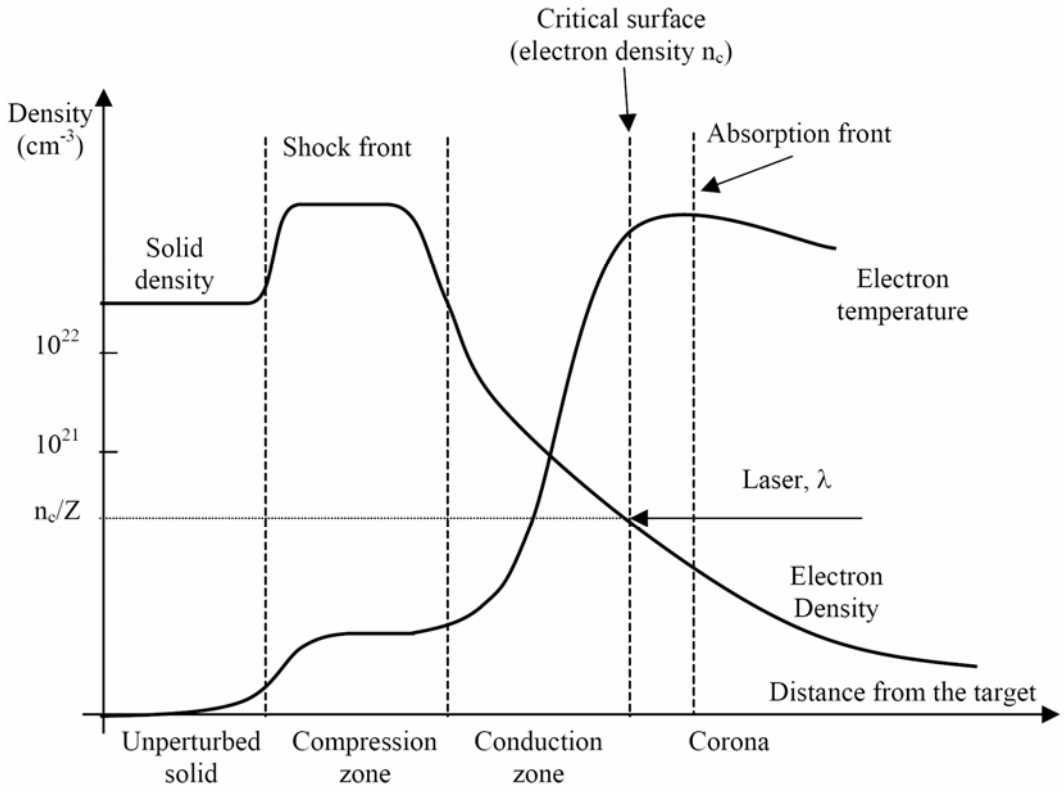

Figure 3 Electron density and temperature profiles in plasma created by a high-intensity laser

$$n_c = \frac{\varepsilon_0 m_e}{e^2}\omega^2 \tag{2}$$

where, m_e is the electron mass, e is the electron charge, ε_0 is the dielectric constant, ω is the frequency of the heating laser and ω_p is the plasma frequency for electron motion relative to the ions in a plasma is given by

$$\omega_p = \left(\frac{n_e e^2}{m_e \varepsilon_0}\right)^{1/2} \tag{3}$$

where n_e is the plasma electron density. The real component of the refractive index n is given by

$$n = \left(1 - \frac{n_e}{n_c}\right)^{1/2} \quad (4)$$

As seen from the equation (4) at the critical density, the real component of the refractive index n = 0.

The laser light is absorbed at electron densities up to the critical density by inverse bremsstrahlung [3] (energy absorption by electrons due to collisions with ions [21]). In the regions with the electron density above the critical density, the pump laser beam does not propagate; it is absorbed near this critical density surface and hence the electrons are mostly heated in the corona zone, which is near the critical density.

The plasma temperature is maximal in the corona zone as can be seen in Figure 3, slightly in front of the critical surface. This is caused by the fact that the laser intensity is gradually absorbed on its path through the plasma and hence the laser intensity becomes weaker than its original value, when it approaches the surface. So, the plasma is heated maximally in the corona zone, where the temperature has its maximum.

The absorbed energy is then transported by thermal electronic conduction both towards the target and the corona. The plasma creates a shock wave that propagates into the target. The target surface ablates under the action of hot electrons and x-ray irradiation from the plasma that also heats the target.

2.2.3. X-ray laser

Extreme ultraviolet or soft-x-ray radiation is often called x-ray laser. The term ‘x-ray’ is more usually thought to apply to wavelengths shorter than 1 nm (photon energy >1 keV). A better term is probably to refer to extreme ultra-violet (EUV) lasers (Figure 4). However, for historical reasons, it is continued to use the term x-ray laser as applied to the wavelength region from 3.5 to, say, 50 nm [3].

Although the x-ray laser is not a classical laser that is composed of an active medium together with two mirrors, it is believed to be a "laser" due to some analogy.

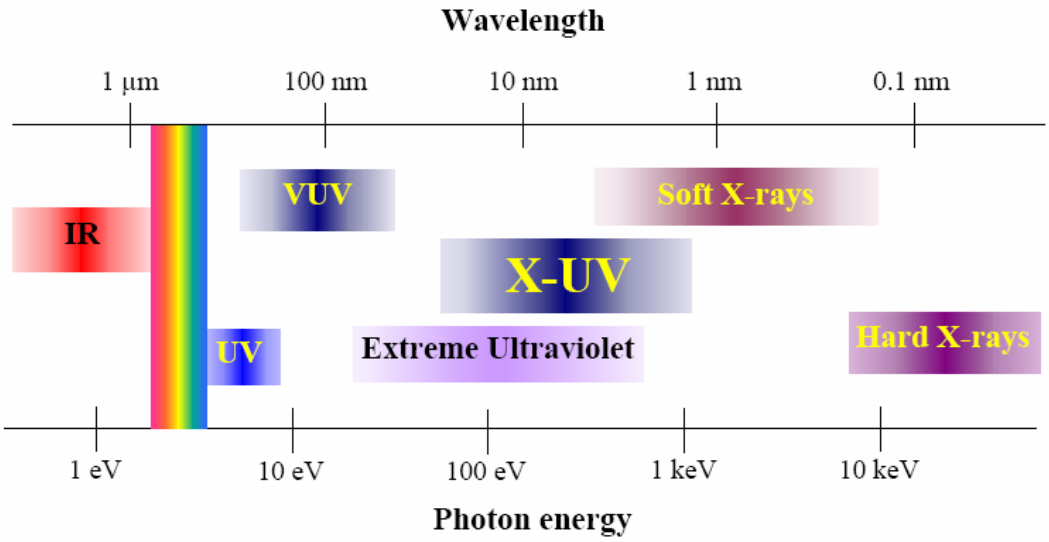

Figure 4 Part of the electromagnetic spectrum, IR is infrared, UV is ultraviolet, VUV is vacuum ultraviolet, extreme ultraviolet is EUV and the X-UV belongs to ~3-60 nm [21]

In a classical laser, the laser beam passes through the resonance cavity, constructed by two mirrors at the end, many times in order to be amplified. When the beam is amplified to a high enough value to lase, it passes through one of the mirrors that is semitransparent. However, in the XUV region (usually 3-60 nm wavelength), the life time of the active medium is not long enough for a photon to pass through several times. That is why, x-ray lasers are operated without mirrors (Figure 5) or sometimes with one mirror that produces a half-cavity [21]. The coherence and uniformity of x-ray laser beams could be improved by reflecting the beam back into the plasma using a single multi-layer mirror [3] as shown in Figure 5.

The x-ray laser results from the regime of Amplified Spontaneous Emission (ASE). In this regime the photons produced by the spontaneous emission are amplified along the plasma column by a stimulated emission [21].

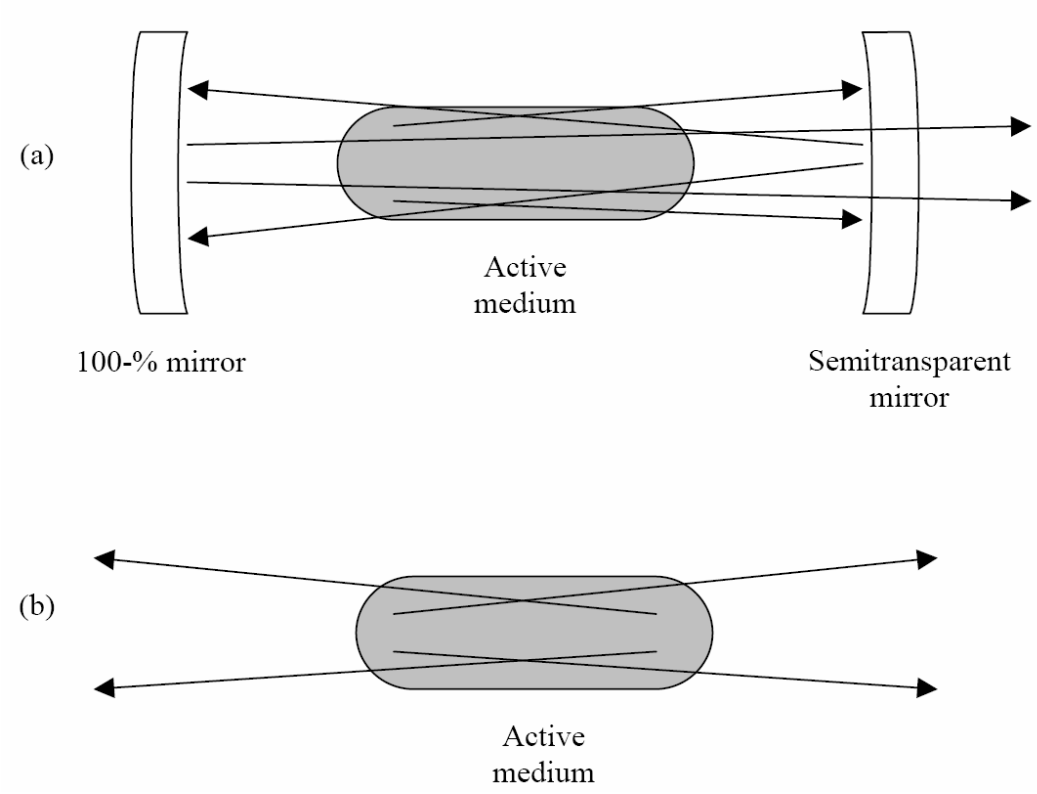

Figure 5 (a) Classical laser, (b) Amplified spontaneous emission [21]

This strong amplification leads the beam act like a laser concerning its directivity, mono-chromaticity and a certain degree of coherence.

The condition for the amplification in the medium is population inversion, the upper electronic level is more populated than the lower one.

To create the population inversion in case of x-ray lasers, in which the levels are very distant from each other, a very strong pump has to be employed. The solution of this problem was found in hot plasma composed of multi-ionized atoms where the transitions between the excited levels correspond to the XUV region. These hot plasmas are usually created by a fast heating process [21].

Ions are not stable as atoms, they have lost their electrons and might have excess energies that make electrons jump to unstable energy levels. However, in order to create the population inversion electrons should be at relatively stable electronic

levels. Since the most stable ions are those with closed electronic shells, they are the most suitable candidate for the x-ray laser experiments. Some popular closed shell types are tabulated in Table 1.

Table 1 Some closed shell ionic types [21]

Ion Type	Closed Shell	Fundamental Electronic Structure	Number of Bound Electrons
Helium (He)-like	n=1	$1s^2$	2
Neon (Ne)-like	n=2	$1s^2 2s^2 2p^6$	10
Nickel (Ni)-like	n=3	$1s^2 2s^2 2p^6 3s^2 3p^6 3d^{10}$	28

For only two electronic levels, population inversion seems not possible since there are no electrons exciting to other levels. That is the coefficient of stimulated emission B_{21} equals to the coefficient of absorption B_{12} (Figure 6).

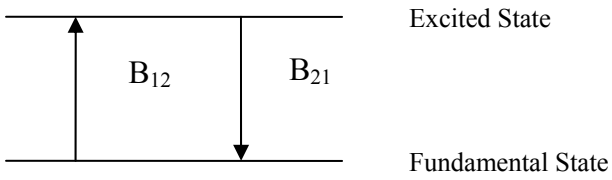

Figure 6 Transition between two electronic levels where B_{21} and B_{12} are Einstein coefficients for stimulated emission and absorption, respectively.

Hence, at least three or four levels are needed for constructing population inversion (Figure 7). The electrons are first pumped from fundamental closed shell state to the excited state 2, so the population inversion between the excited state 2 and excited state 1 is created. This excited state 2 is chosen to be a metastable with respect to the radiative decay, where the excited state 1 rapidly de-excites.

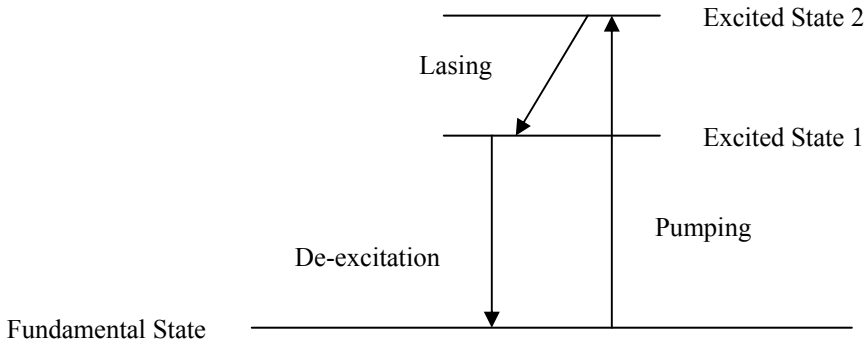

Figure 7 Transitions between three electronic levels

On the other hand, population inversion can be obtained by recombination. In this case, 3 excited states take role, the electrons at excited state 3 recombines and populates excited state 2. Still the excited state 1 is less populated; the population inversion occurs between states 2 and 1. Rest of the procedure is the same.

A high energy density is required to produce x-ray lasing. There is a requirement to ionize a material sufficiently to have energy level separations corresponding to the soft x-ray photon energies [3]. Usually for x-ray laser, the collisional excitation is the mechanism used to excite an electron from the fundamental state to the upper laser state (i. e. to pump the laser) [21]. The collisional excitation is accomplished by high temperature free electrons in plasma that collide with ions. To find a convenient ion, some levels have to be populated from the fundamental state by the collisional excitation. The x-ray lasers arise because monopole excitation in neon- and nickel-like ions to some quantum states is not balanced by radiative decay [3]. The de-excitation from the excited state 2 to the fundamental state is forbidden, while the transition from the excited state 1 to the fundamental state is of a great probability, as a result, population inversions can be produced.

Two different types of ions that use this mechanism for population inversion are nickel-like and neon-like ions. Ne-like and Ni-like ions with closed shells of principal quantum number n=2 and n=3, have been observed to lase with

collisional excitation pumping. The pumping mechanism was first proposed for neon-like ions in the 1970s [14], but lasing was not observed until 1985 [1].

The related transition for Ne-like ion is 3p-3s and for Ni-like ion is 4d-4p. In the Ne-like ions the lasing transitions are identified as $2p^5 3p \rightarrow 2p^5 3s$ (Figure 8) and in Ni-like ions, it is $3d^{10} \rightarrow 3d^9 4d$ (Figure 9).

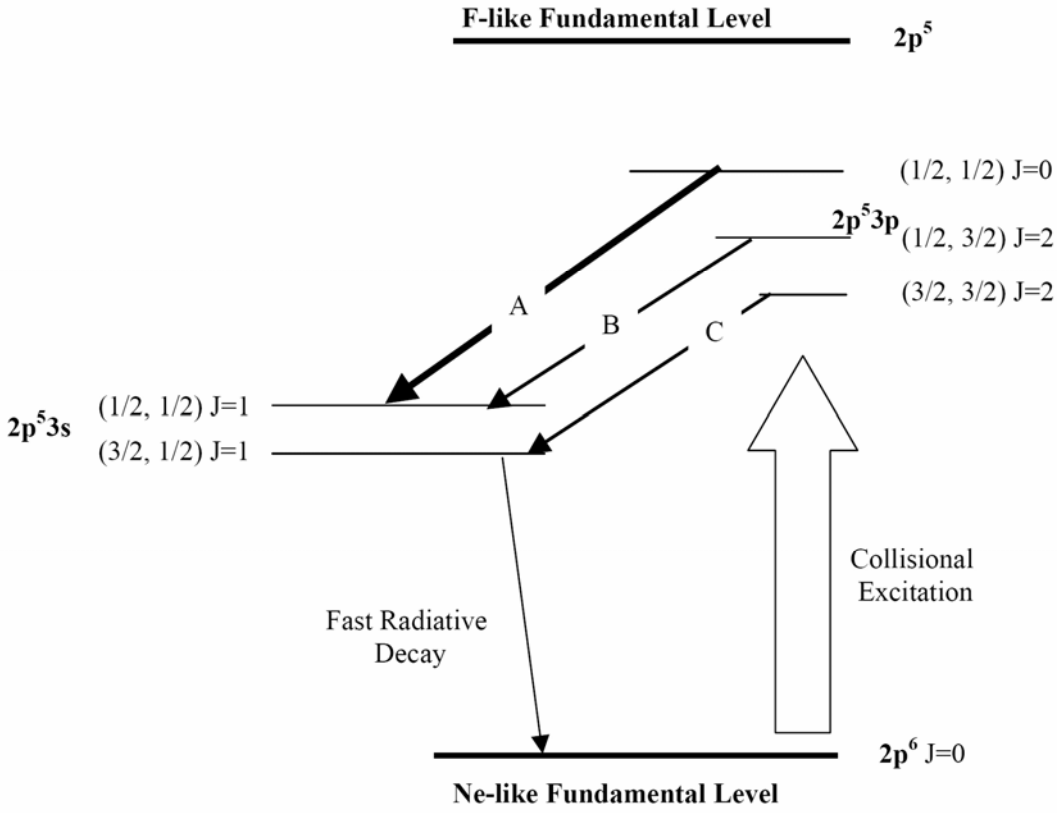

Figure 8 Ne-like ion transition [21]

2.2.4 Comparison of Ne-like and Ni-like X-ray Lasers

As previously stated, collisional excitation from the ground state to the upper laser level of both neon- and nickel-like ions occurs between two levels for which radiative dipole transitions are forbidden. However, the electron collisional excitation from the ground state to the upper lasing level occurs due to monopole excitation at a comparable rate to the collisional excitation for a strong electric

dipole transition [14]. However, lasing in the nickel-like ions has a higher quantum efficiency than for neon-like ions. Here, the quantum efficiency is the ratio of the laser photon energy to the energy of the upper laser level above the ground state (the level pumped by collisional excitation). Principally because of the enhanced quantum efficiency, lasing at shorter wavelengths has been observed with nickel-like ions [3].

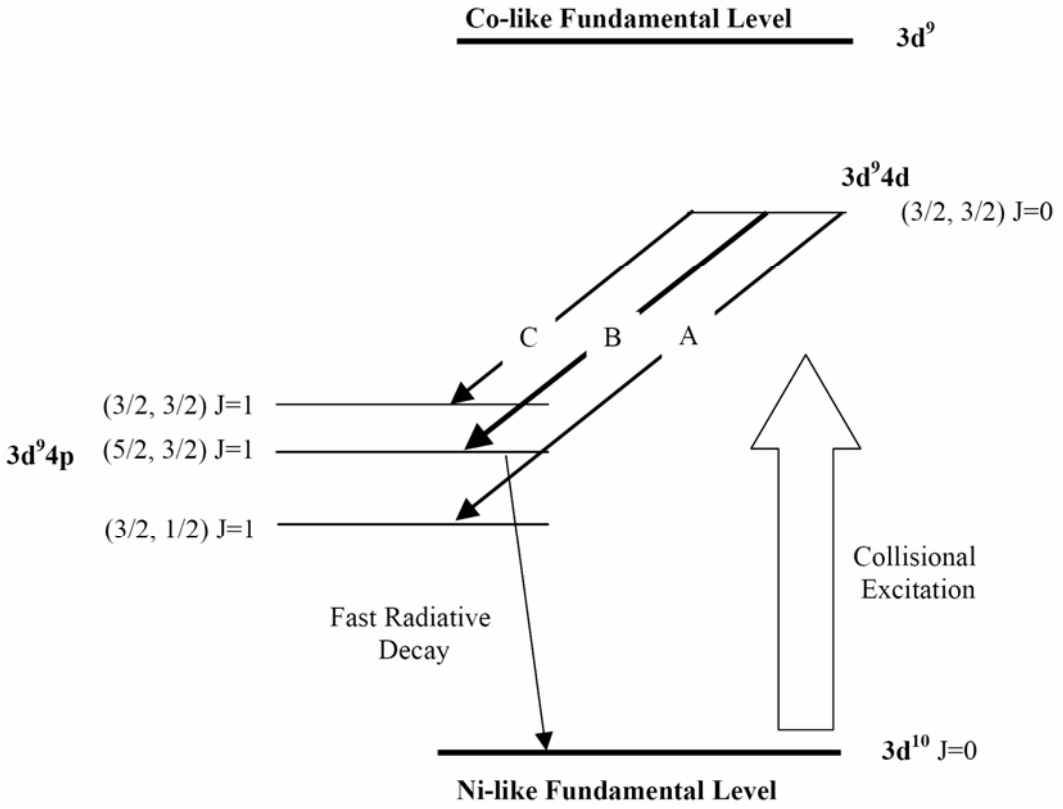

Figure 9 Ni-like ion transition [21]

Schematic energy level diagrams for neon-like and nickel-like quantum states involved in lasing are shown in Figure 10.

McCabe et al. [22] by the means of a zero-dimensional (0D) version of the full EHYBRID code (Section 3.3), compare the operation of the Ne-like Ge [23] and Ni-like Gd [22] schemes.

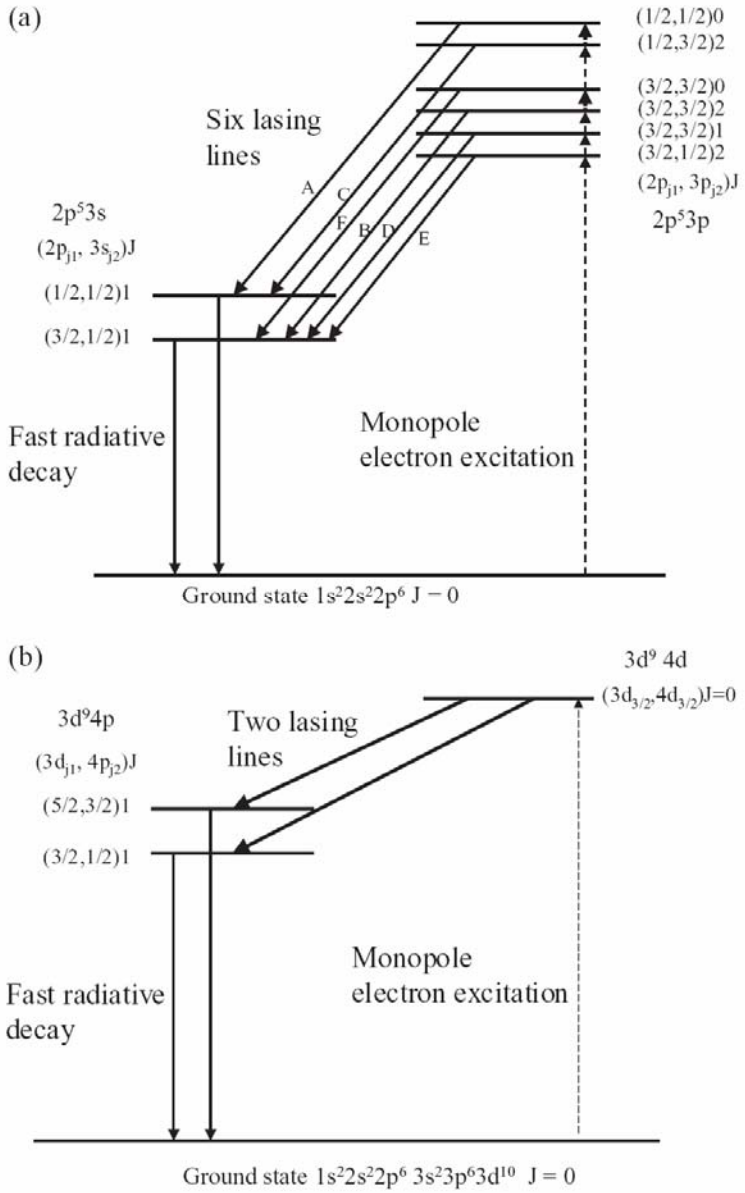

Figure 10 Schematic energy level diagram of (a) Neon-like lasers and (b) Nickel-like lasers [3].

In order to systematically investigate the temperature and density space of the plasma and the operation of the Ni-like scheme, McCabe et al. [22] used a 0D code. This code is a subset of EHYBRID running in a single cell with the hydrodynamics routines switched off and no electron-ion thermalization. The full collisional-radiative model is used. The electron and ion temperatures and the ion density are all fixed. The output is therefore the response of the system to an

electron temperature step function. The ion temperature was set independently in those simulations to 150eV.

Ge and Gd are superficially similar and they performed identical simulations for Ge and Gd. The upper lasing levels are 1337 and 1340 eV, and the ionization energies for the Ne-like and Ni-like ion stages are 2192 and 2630 eV, respectively. That is why they have chosen them for a comparative computational study [22].

McCabe et. al. [22] examined the germanium results shown in Figure 11 with a similar Figure 12 (Holden et al). They included dielectronic recombination and used a more detailed model of the Ne-like ionization stage, in order not to make the identical treatment. The inclusion of dielectronic recombination increased the relative population of Ne-like ions in the equilibrium plasma, and this was reflected in the slower rise of average ionization predicted in their 0D (dimensionless) calculations.

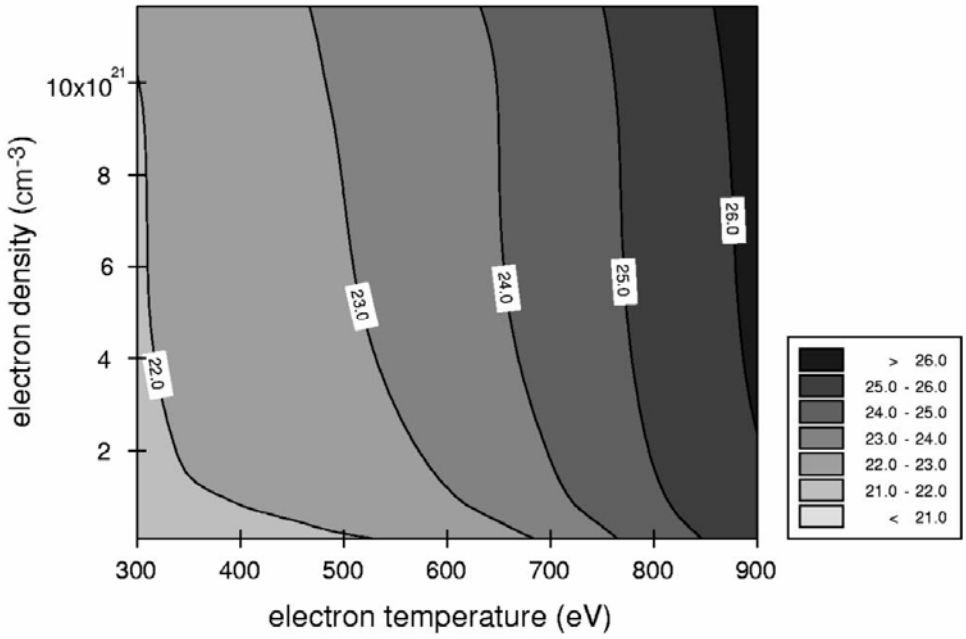

Figure 11 Steady-state ionization and balance average ionization [22]

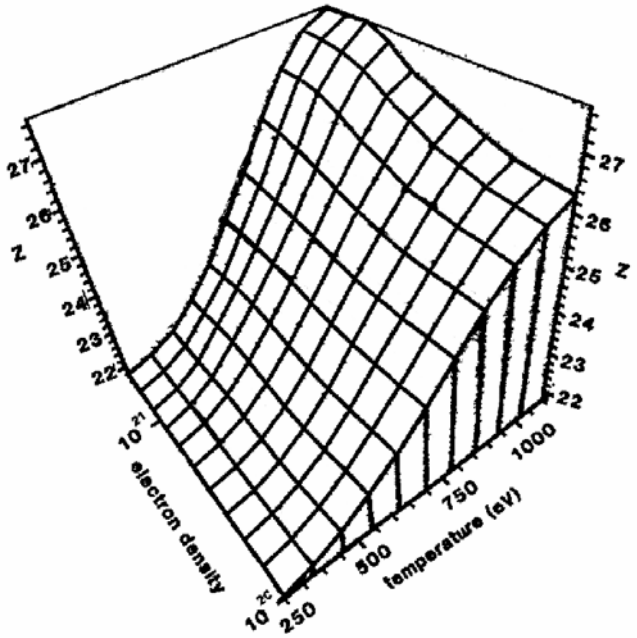

Figure 12 Steady-state ionization balance as a function of electron density and temperature [23]

Their 0D calculation, as figured in Figure 13, showed the gain in the steady state with the ionization balance included. This indicated an optimum electron temperature of 500 eV at an electron density of 10^{21} cm^{-3} with a peak gain <20. On the other hand, Figure 14 showed the peak gain achieved while the system was ionizing. This shifts the optimum conditions to higher temperatures and slightly higher electron density, but also indicated that much higher gains may be achieved in this regime.

As the case for Ge by Holden et al. [23], the optimum gain conditions do not coincide with those conditions which produce a suitable steady-state ionization balance. That is the primary conclusions drawn for Ge by Holden et al. [23] are equally valid for Gd by McCabe et al. [22].

However, a striking difference was the relative instability of the Ni-like ionization stage. The contour plot in Figure 15 for average ionization as a function of temperature and density showed that clearly. The relevant ion stages of interest were Ne-like Ge (Z=22) and Ni-like Gd (Z=36). Contour lines indicating an

average ionization of 22 and 36 traverse almost identical paths in the temperature density plot. Following lines of equal electron density, Gd reached a Co-like average ionization after an average temperature increase of 50 eV. Ge was significantly more stable, requiring a 200-eV rise in electron temperature to increase the average ionization by one [22].

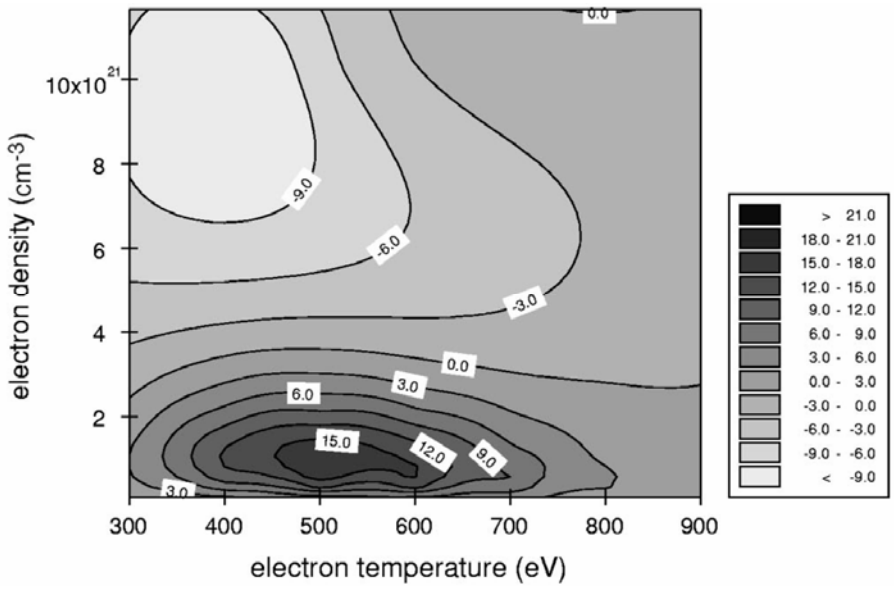

Figure 13 Ge equilibrium gain (cm^{-1}) [22]

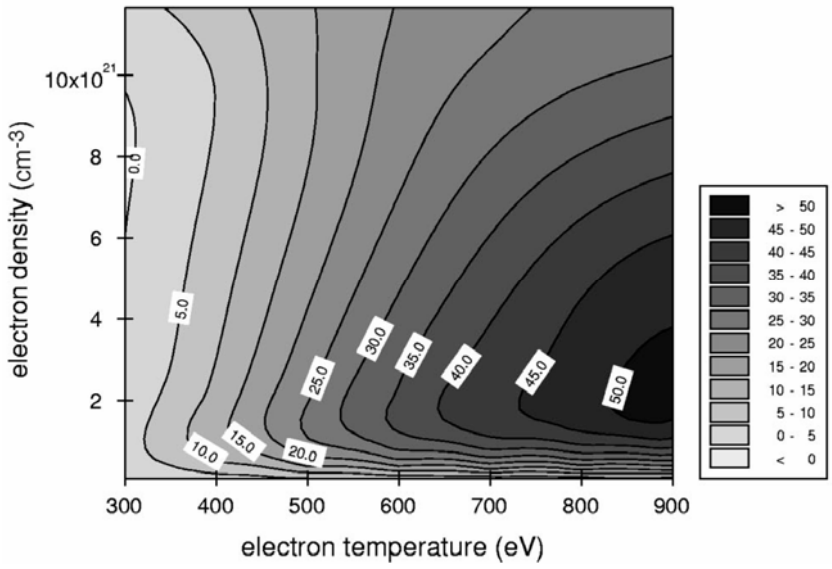

Figure 14 Ge peak transient gain (cm^{-1}) [22]

The relatively rapid sweep through the Ni-like stage is emphasized by the steady-state gain calculations (Figure 15). This indicated that a significant Ni-like Gd population occupies a much smaller region of the parameter space investigated. These data underline the Ne-like Ge conclusion that the conditions for a steady-state ionization balance dominated by Ni-like ions is significantly different from the conditions required for optimum gain. The peak gain plot for the ionizing plasma (Figure 16) is an accurate indicator of the conditions required for lasing [22].

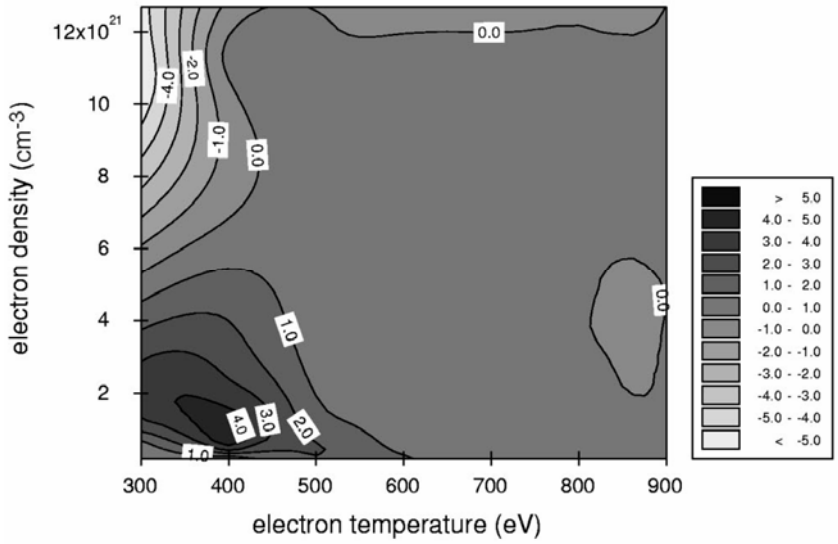

Figure 15 Gd equilibrium gain (cm^{-1}) [22]

The relative instability of the Ni-like ion stage is a result of the larger collision cross section of excited states having a higher principal quantum number compared to the Ne-like scheme for the lasing levels. The monopole excitation rate into the upper lasing level of Gd is greater than twice that of the Ge upper lasing level. The large electron impact cross sections increase stepwise excitation through the n=4 and higher manifolds, adding significantly to the ionization rate. The increased ionization is very significant for the stability of the lasant ion stage. As a result the Ni-like ion stage burns through very rapidly, leading to overionization in a very short time [22].

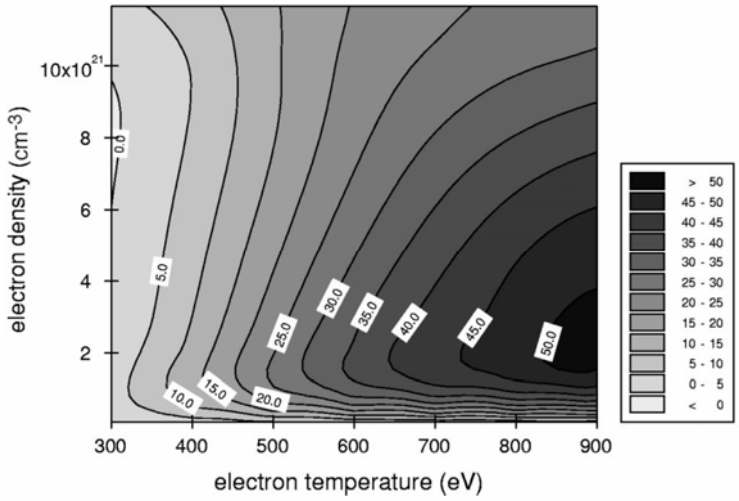

Figure 16 Gd peak transient gain (cm^{-1}) [22]

A contour plot of gain as a function of electron density and temperature (Figure 16) indicates a usable parameter space not dissimilar to Ne-like Ge shown in Figure 14. The predicted gains are also similar in magnitude. This is a reflection of the higher pumping rate into the upper lasing level maintaining gain despite the smaller Ni-like ion population. As expected, the temporal evolution of the gain in Gd is faster reflecting the rapid ionization rate. Using as an example an electron density of 10^{21} cm^{-3}, and an electron temperature of 800 eV the temporal full width at half maximum (FWHM) of the Gd gain profile is half that of Ge (Figure 17). It can also be seen that the Gd gain returns to zero, indicating that at this temperature the Ni-like ion stage is depleted in the steady state [22].

At this point, investigating Ni-like Sn with relatively high Z (atomic weight=50 amu) seems challenging. In order to investigate high Z atoms and create x-ray lasing ordinary approaches may not be sufficient. One way to obtain x-ray from such atoms is to use prepulse which will be discussed in Section 2.4.1.

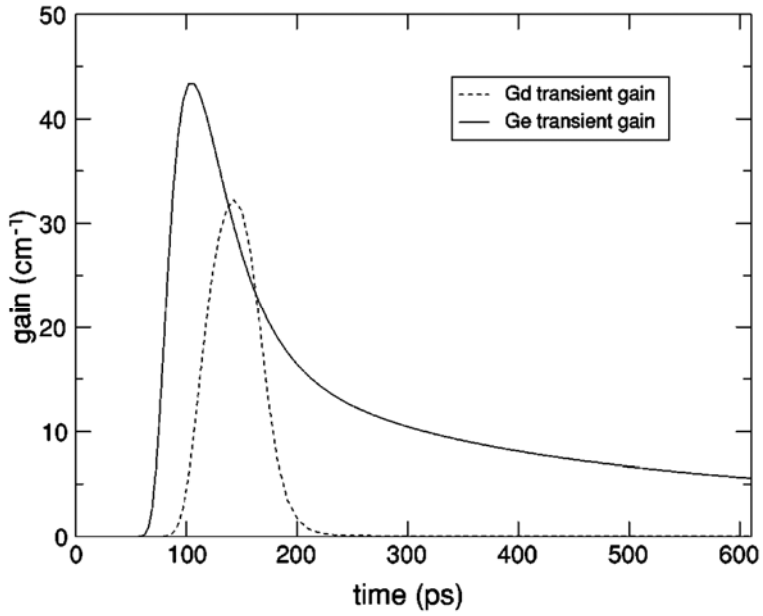

Figure 17 A sample plot of the temporal evolution of gain from the steady-state calculations. The electron temperature is 800 eV and the electron density is 10^{21} cm^{-3} [22].

The high Z, Ni-like ions can lase at very short wavelengths that make them more popular than Ne-like light ions on some applications. Biological usage and EUV lithography are the common examples. Another reason to investigate tin is, it is one of the preferred atoms for EUV lithography (Section 2.3.1).

2.3. Application of X-ray Lasers

Some of the potential and realized applications possible with x-ray lasers are x-ray lithography (detailed in Section 2.3.1), x-ray spectroscopy, x-ray microscopy [24], scanning and holographic microscopy [25], the interferometric probing of long lengths of high density laser-plasmas [3], such as inertial confinement fusion research, the production of high energy particles and gamma rays [3].

Moreover, x-ray regime radiation is important because at these wavelengths water becomes transparent and that facilitates the probing of living organisms [18]. The study of radiation damage to biological cells [24], the study of the biochemistry of DNA damage and repair [25] are also potential application areas for x-ray.

2.3.1. Lithography

Extreme-ultraviolet lithography (EUVL) which is a technology, capable of creating nanometer-scale patterns for use in semiconductor manufacturing and so on, [26] is nowadays considered as an attractive candidate to succeed conventional optical lithography.

To enable this technology, a reliable source is required that consistently provides sufficient and clean power at about 13.5 nm to yield adequate wafer throughput in a manufacturing tool [27]. The source can be synchrotron radiation, discharge produced plasma (DPP) and laser-produced plasma (LPP). The use of synchrotron radiation as the light source is not practical considering the cost as well as the size and complexity [27]. EUV sources based on LPPs have several advantages over discharge-based EUV sources that include power scalability through the tuning of laser parameters, good dose control, flexibility in dimensions, spatial stability, minimal heat load and a large solid angle of collection [27]. The favorable technology is the laser-produced plasma (LPP) in which intense laser light incident on a solid target surface in vacuum generates x-ray emitting plasma [28].

Different targets were considered for generating 13.5 nm plasma emission including lithium, xenon and tin. Lithium plasma exhibits strong Lyman-α emission of Li^{+2} at 13.5 nm [29]. The conversion efficiency (CE) obtained with different Xe target plasmas is ~1% which is not enough for commercial lithography production purposes [27]. Laser-produced tin plasma is considered to be an ideal source for EUVL as it provides a CE better than 3% [30]. That produces another valid reason to examine tin plasma in this study.

Spitzer et al. [28] in 1993, determined the absolute conversion efficiency from laser light into x-rays for various target materials, laser wavelengths 1064 nm and 532 nm, pulse lengths 7.5-30 ns, incident intensities $1x10^{19}$ - $1x10^{13}$ W/cm^2 and spot sizes 15 μm - 2 mm. Laser source parameter ranges have been identified to produce optimal x-ray CE at 13.3 nm for Sn targets. The measured CE for Sn

meets the necessary EUVL system requirements. They conclude that Sn is an efficient target to convert Nd: YAG radiation to around 13 nm EUV radiation, achieving over 2% conversion efficiency [28].

Tin plasmas characteristically emit broadband spectra around 13.5 nm that originate from many different ionization stages [29], mostly Sn^{+8}, Sn^{+9}, Sn^{+10}, Sn^{+11} are the ions that form desired x ray [31]. However, during this x ray formation, one of the most important problems is encountered. It is the debris from the plume from a laser-produced plasma source for EUVL. In general, the debris from laser-generated plasma can include energetic ions, neutrals, particulates, and molten droplets [32]. To prevent damages several methods including tape targets, electrostatic repeller fields, the addition of ambient gas [32] and application of magnetic fields are tried. Another method of restricting debris is to use the minimum amount of Sn atoms required for sufficient EUV emission.

It has been shown numerically that the tin ion distribution was not significantly changed when the concentration of tin dropped from 100% to 1%. Harilal et al [29] indicated that the density of tin necessary to obtain bright emission at 13.5 nm is around 0.5% when they are aiming is to maximize the efficiency of EUV emission from tin doped foam targets while minimizing the number of tin atoms.

In another study of Harilal et al [32], mitigation of the debris is attempted to prevent by an ambient gas. The use of an ambient gas environment for controlling highly energetic particles from a tin plume can be an effective way, since ambient gas species act as a moderator for the energetic plume species during the flight time from target to substrate.

Hydrogen, helium, and argon gases provide exceptionally good transmission to 13.5 nm compared to other gases. Being lighter in mass, a hydrogen or helium ambient environment may require higher pressures to control energetic tin ions and other particulates emanating from a laser-produced tin plasma. At a particular pressure, being heavier, argon (atomic weight=40 amu) is expected to be more

effective for slowing down the energetic ions and atoms in comparison with hydrogen or helium ambient. Because of this reason Harilal et al. used argon gas as an ambient for controlling the various species from the tin plasma.

They used a 1064 nm, 10 ns (FWHM) pulses from an Nd: yttrium aluminum garnet (YAG) laser to create tin plasma in a stainless steel vacuum chamber (~10^{-6} Torr). The laser beam, at normal incidence, was focused onto the target using a plano-convex lens to a focal spot diameter of 60 μm [32] ($4x10^{11}$ Wcm^{-2} was used for all measurements).

Monte Carlo simulation results showed that with this ambient pressure, the tin species with kinetic energies less than 5 keV could be effectively stopped before reaching the collector mirror in a EUVL source setup. Their experimental results have clearly highlighted the influence of ambient argon gas on tin plume kinetics and dynamics even at distances less than 25 mm from the target [32].

Generally, in a EUVL tool, the collector mirror is expected to be placed ~15–20 cm from the plasma source. For industrializing EUVL, a lifetime of more than 10^9 shots is needed for the collector mirror. So tin is the best target when the debris from laser plasma is controlled to create a clean photon source for EUVL.

2.4. Laser Pumping Configurations

Starting primitively, in order to ionize an atom, high enough energy to release electron should be transferred to it. To obtain plasma medium by the means of a solid target needs much more energy. When x-ray comes to the point of view, there should be efficient energy to make x-ray laser. It can be done in different ways, one of which is lasing the target intensely.

The laser pulse which could lead x-ray lasing should be very energetic, in order not to try to obtain much energy from a pulse, multipulse [33], prepulse, long pulse short pulse combination could be used [15]. They are the quasisteady state

(QSS) inversion schemes which will be explained in Section 2.5. Another way, after femtosecond pulse laser are come to the stage, is transient collisional excitation (TCE) (Section 2.5.).

Lasing Sn target with only one pulse, and with prepulse-main pulse combination-TCE cases are simulated in Chapter 4.

2.4.1 Prepulse

Prepulse is used to generate long scale length plasma. This reduces refraction effects and increases the laser source size. The second pulse is used to pump the plasma to sufficiently high temperatures for lasing. The timing of the second pulse and the relative power of the prepulse are variables in a large parameter space [22].

McCabe et al., run some simulations accordingly with experiments using VULCAN laser system at Rutherford Appleton Labs to discuss the role of the prepulse. In their experiments, the maximum energy in a single pulse was 60 J for 70–100-ps pulses into a 2-cm line focus. They limited the prepulse fraction between 1% and 33% of the main pulse maximum energy.

Figure 18 shows the expansion of a Gd target driven by 0.4-, 2-, and 13-J prepulses over a period of 7 ns. Radial expansion was measured from the target back surface. That explains the 20-mm offset of the radial expansion axis.

The smallest prepulse, plot (a), barely starts the expansion process. The preplasma has an initial maximum electron temperature of 25 eV and an average ionization of less than 15. As this layer expands away from the surface it cools and recombines, and the ion density drops. The electron density of the expanding plume rapidly becomes too small (~10^{18} cm^{-3}), more than 100 mm from the surface for significant inverse bremsstrahlung absorption. Therefore, a second laser pulse will be absorbed in a layer that remains close to the target surface. This

region has very low ionization (~4) and temperature (~6 eV), but this is offset by a high ion mass density between 0.1% and 1% that of solid suitable for collisional pumping. To generate a good signal the radial extent of the region needs to be of the order of 50 mm to produce a reasonable source size. This explains the long optimal pulse separations obtained in experiments at low prepulse levels [22].

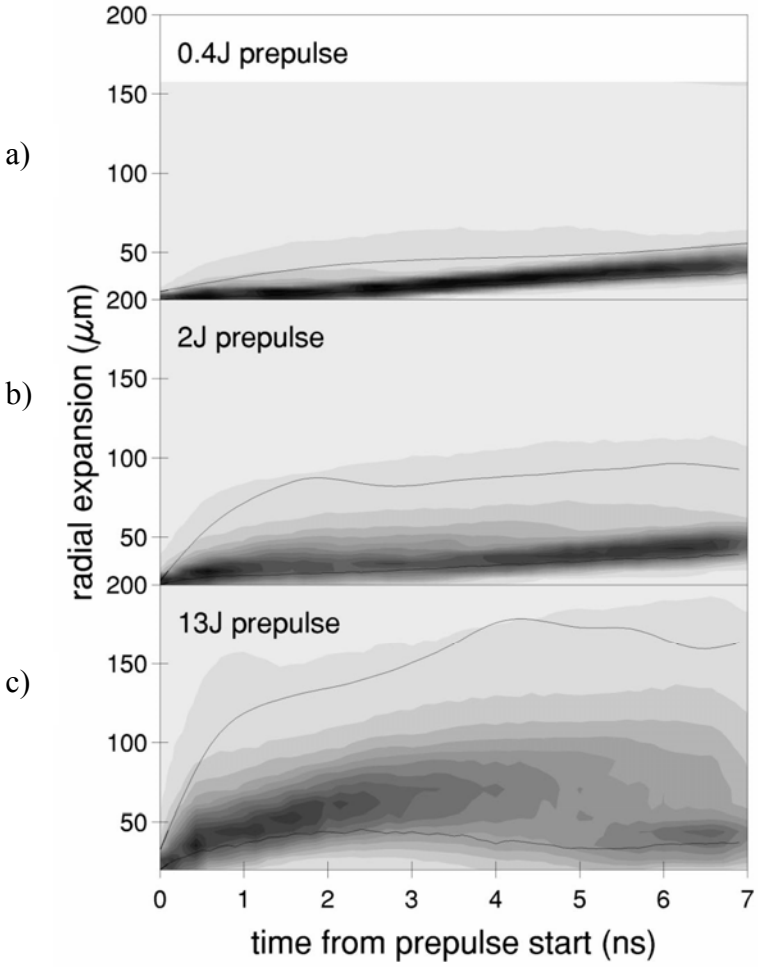

Figure 18 Evolution of the plasma and corresponding absorption region. The shading indicates where laser energy would be absorbed at the onset of a driving pulse. The bounding lines indicate the region in which 90% of the laser energy would be absorbed [22].

For larger prepulses optimized conditions occur when the initial high-density layer has expanded and cooled sufficiently to form a large enough low-density

gradient region to minimize refraction and maximize the source area. As this region continues to expand the electron density will decrease until it is relatively transparent to the pump pulse. At this point the expansion behind the plume will absorb most of the pump energy. This process can be seen in plot (c) of Figure 18 for the 13-J prepulse. Initially very hot rapidly expanding plasma was generated [22]. The hot plasma expanded and cooled, and within the first 3 ns a large region of uniform absorption was created. After this time the rapid expansion and cooling reduced the electron density such that pump pulse energy was being dissipated over a larger volume such that both the local temperatures produced and laser gain were reduced.

The 13-J prepulse is large enough to detach the absorption region from the surface, where the 2-J prepulse is not sufficient.

Also a significant point is that, in both cases, the smaller the pulse the earlier it must arrive to achieve optimum lasing; otherwise the density at the energy dump will drop below the critical level required for lasing. That explains the importance of the prepulse.

Another comparison can be done by investigating pulse energy altering. McCabe et al. [22], studied this with pulses that have energies 0.4, 2, and 13 J, respectively and they have also run simulations for this prepulse level with the main pulse reduced to keep the total energy constant (Figure 19).

The data clearly indicate that the optimum pulse separation increases with decreasing prepulse level. It also predicts that for a specified main pulse energy, increasing the prepulse energy will increase the laser output within the bounds of their simulation [22].

Moreover, Li et al. [34] noted that the demonstration of gain in Z around 50 amu nickel-like ions may lead to significant progress in developing a small scale system operating at short wavelengths. This motivated them to investigate x-ray

lasing in nickel-like tin, which is the one of the motivation source for this thesis to investigate tin.

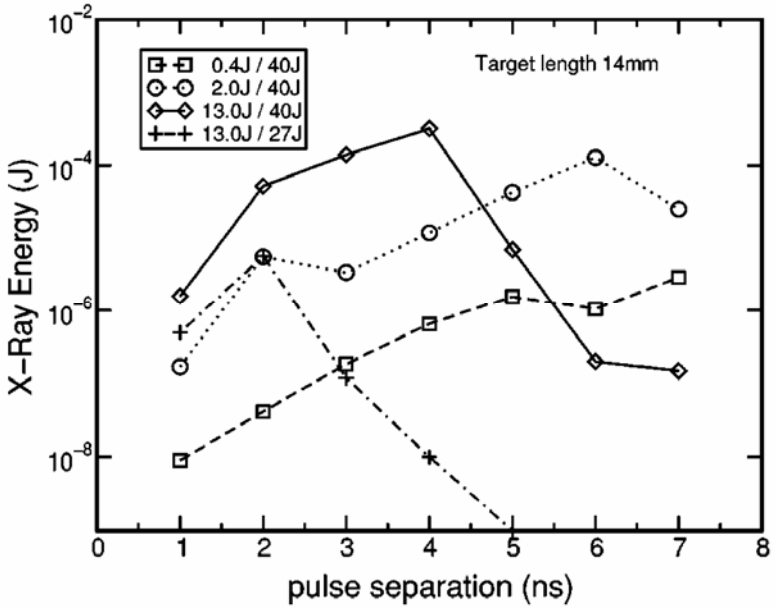

Figure 19 Gadolinium dual 100-ps pulse optimization curves for a 14-mm target. Four different main and prepulse configurations are contrasted [22].

Li et al. [34] at Max-Planck-Institut für Quantenoptik, used two techniques in their experiment for gain demonstration. One is the prepulse technique, which has been successful in producing low-Z Neon-like lasers. The other is the use of curved targets, which has been proven to be efficient to enhance the J=0 →1 laser in Neon-like Germanium and in Nickel-like Lanthanide ions. With these techniques, a 3-cm-long target of 1 m radius of curvature irradiated by the Asterix iodine laser at 1.315 mm with a total energy of 500 J and a 7.5% prepulse [34], they observed x-ray lasing in nickel-like tin with a gain length of 4.8.

As a conclusion, the shortest wavelength laser produced so-far at 3.5 nm was similarly created using the NOVA near-infrared laser incident onto a foil target [3]. Laser-plasmas also have the record for the shortest wavelength saturated laser at 5.9 nm [3]. This was achieved using the VULCAN laser at the Rutherford Appleton Laboratory with enhanced efficiency and much smaller laser energy due

to the use of a pre-pulse forming a pre-plasma into which the main pumping laser pulse interacts.

A computational investigation of the Ne-like Ge collisionally-pumped laser was considered by Healy et al. [35] by the means of the EHYBRID code to understand the role of prepulses. It has been shown that the absorption of the pumping laser is enhanced by the prepulse, and less of the absorbed energy is expended in the plasma expansion, resulting in better coupling to the free electrons and more ionization within the plasma [35].

2.5. Quasisteady State versus Transient Collisional Excitation

Very short high-intensity pump pulses produce rapidly ionizing plasmas with potentially high gains for short times. Such pumping schemes are commonly referred to as transient collisional excitation schemes [22].

From the first demonstration of soft x-ray lasers in 1985 [36], quasisteady state (QSS) collisional x-ray lasers have been investigated intensively. In the QSS scheme, very energetic long pulse is focused onto a foil or slab target in order to first, vaporize the target, then ionize it to form plasma and finally produce population inversion [37]. By comparison, the transient collisional excitation (TCE) was proposed as an alternative scheme to significantly save drive energy [38].

According to the theory of Afanasiev, the population inversion in the TCE scheme appears to be due to the different transient pump rates of the energy levels [38]. The analytical approach for TCE was performed in an ideal model: the electron temperature has a sudden jump to high value during a very short time and then becomes constant. The ionization process can be ignored. During the pump time, the theoretical estimate of transient gain can be high [38].

To make the TCE scheme work we must replace the single main pulse with two pulses. A short pulse alone is not sufficient. The reason for this is that the main pulse in the QSS scheme has dual role: first to heat the expanding and cooling plasma to the correct ionization stage, and second to pump the upper lasing level. The TCE schemes break this process into two separate stages using two pulses: a longer low-intensity pulse and a very short high-intensity pulse [22].

On the other hand, it should be noted that TCE experiments using pulses on the order of 1 ps, for Ne- and Ni-like schemes indicate that a prepulse is not always required for optimal lasing [22]. However, in a study with a CPA pulse by Simms et al. [39], gadolinium produced largest output powers and intensities when pumped by two long pulses, both of peak intensity of $8x10^{12}$ Wcm^{-2}, with 2 ns separating them, and the CPA pulse added 220 ps into the second pulse.

In the simulation explained in Chapter 4, it is shown that with a peak intensity of $3.83x10^{7}$ W/cm^{2} with a 2ns-pulse is enough to remove 22 electrons from tin target, however that is not the only requirement for x-ray lasing. Therefore CPA technique is the preferable way to have x-ray lasing which is simulated and also discussed in Chapter 4.

The TCE scheme differs from quasi-steady state (QSS) in a number of areas, but mainly because the rise time of the level excitation rates is shorter than the collisional excitation time scales. In QSS scheme, the main heating of the preformed plasma occurs on a time scale shorter than the relaxation time of the lasing levels; however, in TCE, CPA (Chirped Pulse Amplification) technology help to heat the preformed plasma with picosecond pulses. Modeling suggests that a large transient population inversion is obtained via collisional excitation from free electrons on a timescale before ionization occur [40]. This produces a short-lived transient population inversion pumped directly from the ground state until collisions redistribute populations among all levels finally achieving the QSS state. As mentioned above, multiple pulses [33], prepulses, and long pulse short pulse combinations are all QSS inversion schemes [15]. Since during the time of

population redistribution the inversion is defined by the upper laser level population, it is predicted that TCE will produce very high gains and, therefore, high efficiency x-ray lasers [38].

In the QSS excitation scheme, electrons at the lower level decay into the ground state due to the strong dipole radiation while the upper level is populated through the monopole collisional excitation. This results in a population inversion between the upper and lower energy levels. In recent years, the QSS is usually reached by using a low intensity prepulse followed by a high intensity main pulse [38].

In experiments the hydrodynamic conditions of the TCE scheme can be realized by using a low intensity long prepulse to produce a preplasma with rich population of Ni-like or Ne-like ions in the ground state. After the prepulse, a high intensity short main pulse is used to make a jump of electron temperature [38]. The CPA laser technology has made the high intensity picosecond and femtosecond pulse lasers available at university laboratories. There will be one at Middle East Technical University (METU) Physics department soon. This situation has created a great possibility to realize TCE x-ray lasers at small laser laboratories, thus making the wide application of x-ray lasers possible.

It is well known that the preplasma for TCE should have a rich population of ground state ions [38]. In order to obtain an optimum peak intensity of prepulse, the simulations have been performed by Lu X. et al., for a 1 ns prepulse with different peak intensities of $1x10^{12}$ W/cm^2, and $5x10^{12}$ W/cm^2. Figure 20 shows the spatio-temporal profile of Ne-like ions fraction in plasmas produced by such prepulses. The peak intensity of prepulses exists at 1 ns in the figures. It is apparent that the $1x10^{12}$ W/cm^2 intensity prepulse is not high enough to ionize the preplasma to a Ne-like state. The prepulse with a peak intensity of $5x10^{12}$ W/cm^2 is enough to generate a rich Ne-like ionization population in the preplasma for a TCE x-ray laser [38].

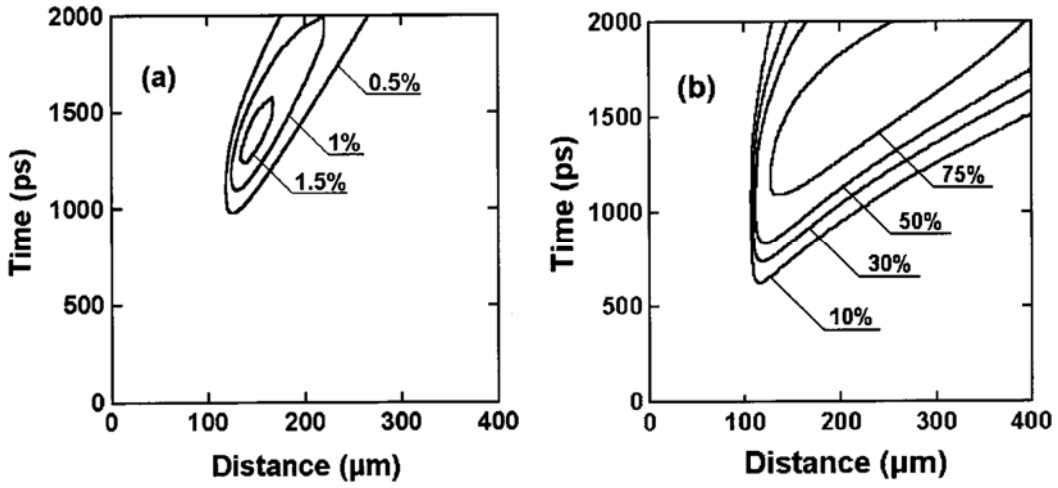

Figure 20 The fraction of the ground state Ne-like ions versus space and time in the plasmas generated by 1ns long prepulses with a peak intensity of $1x10^{12}$ W/cm^2 (a) and $5x10^{12}$ W/cm^2 (b). The initial position of target surface is located at 100 μm [38].

In order to see the difference between TCE and QSS excitation Lu X. et al. [38] did calculations with different main pulse duration but a fixed energy. The 1D Lagrangian hydrodynamic code MED103 was used. The main pulse durations used in the simulations are 50 ps, 5 ps, 500 fs, and 50 s. The peak intensities of the main pulse are 10^{14} W/cm^2, 10^{15} W/cm^2, 10^{16} W/cm^2, and 10^{17} W/cm^2. All simulations performed with a 1ns prepulse at $5x10^{12}$ W/cm^2. The peak to peak time delay between the prepulse and main pulse was set to be 0.5 ns. The main pulse reaches its peak intensity at 1500 ps on the time scale used in Figure 21.

It is apparent that the characteristics of the x-ray laser driven by a 50 ps main pulse are a typical QSS case. The high gain of 83 cm^{-1} is due to the high density of Ne-like ions in plasma. In case of 5 ps drive pulse, the electron temperature increases rapidly from; ~200 eV to 2.2 keV near the critical density, and from 400 eV to; ~1.5 keV in the corona region of $n_e > n_c$ when the main pulse comes [38]. During the main pulse pumping the ion temperature is almost unchanged, 15% ions are over-ionized to F-like state.

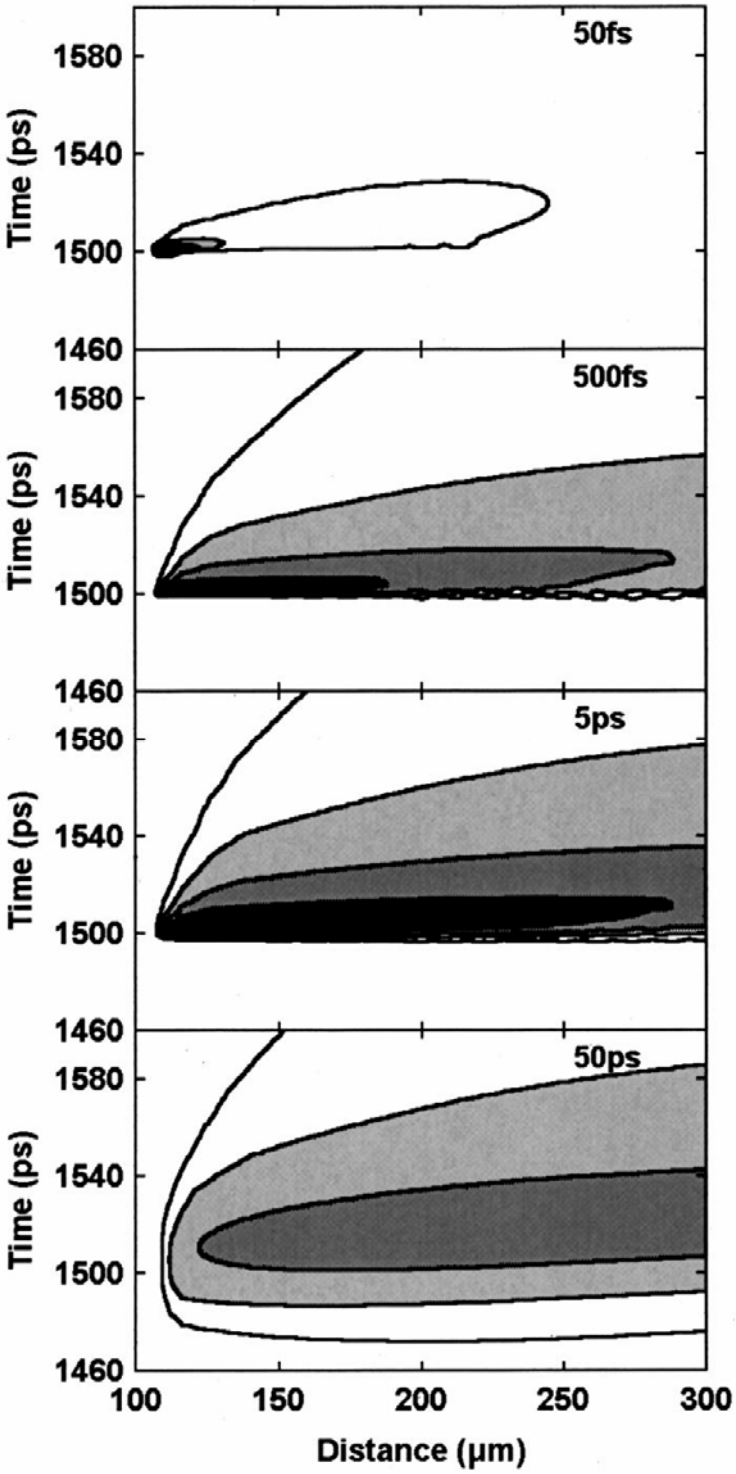

Figure 21 Contours of electron temperature versus space and time of the four values of the drive pulse durations 50 fs, 500 fs, 5 ps, and 50 ps. The electron temperature in plot reduces from 1500 eV (black) to 600 eV (white) by step of 300 eV [38].

So they believed that for Ne-like Ge x-ray lasers, the so-called ‘‘TCE’’ scheme, which uses picoseconds pump pulses, has no difference from traditional QSS excitation in the framework. The high gain of short pulse driven x-ray laser is only due to the relative high electron temperature [38]. A similar calculation with a different hydrodynamic code is done for Ni-like Sn which will be discussed in detail at Chapter 4.

In conclusion, they have investigated the Ne-like Ge x-ray laser at 19.6 nm numerically using a one-dimensional hydrodynamic code MED103 for a 100 mm thick Ge planar target irradiated by a nanosecond prepulse followed by a short drive pulse with different durations but a fixed energy. The comparison of ionization balance created by different drive pulse shows that in the dynamic range from 500 fs to 50 ps, the transient collisional excitation does not exist. The real transient x-ray laser of Ne-like GE at 19.6 nm wavelength can only be generated by a short laser pulse with tens of femtosecond duration [38].

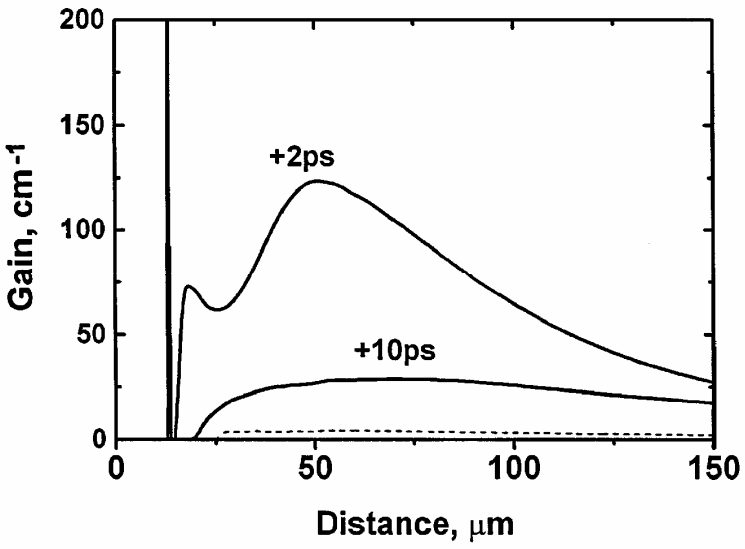

Figure 22 Transient $J = 0 \rightarrow 1$ gain profiles as calculated by the code RADEX at 2 ps (+2 ps curve), 10 ps (+10 ps curve) after arrival of 1ps laser pulse and the QSS gain is shown at 2 ps (dashed curve) [15].

In the study of Dunn et al. [15], QSS scheme is compared to TCE scheme in terms of gain profiles by the means of RADEX code. In their calculation, a formation pulse of 1 ps is used to heat a solid planar target and produce long scale length plasma. After that, two different pulses, 2 ps and 10 ps, are tried to investigate them. Another investigation which involves the comparison of QSS and TCE schemes is also included with only one pulse at 2 ps (Figure 22).

As clearly seen from the Figure 22, the QSS gain (dashed curve) at 2 ps is substantially lower than the transient gain [15].

CHAPTER 3

MODELING METHOD

Modeling is a tool for investigating the experiment before it is performed. It provides to check whether the input data are satisfactory or not, by means of this prescience the experimental set-up together with time can be saved. Moreover, it helps to decide the experiment in detail and calculates some quantities that cannot be directly measured. Besides, data from the experiments can also be investigated.

Before performing the matter-laser interaction, plasma and x-ray production and x-ray laser experiments, commonly, some computational work is done to be aware of the proper data input. There are some modeling techniques some of which will be explained in few words.

In this chapter, techniques for plasma modeling will be briefly explained and then some detailed information on one of the modeling techniques, hydrodynamic modeling, together with a raytracing code will be mentioned. Finally, operation style of the EHYBRID code which is used in this study will be discussed (for further information Pert 1994).

3.1 Plasma Simulation Techniques

There are several examples of plasma simulations in recent literature, differing in the theoretical approach, the method of solution etc. A most general classification of plasma models is:

- Models based on experimental measurements
- Self - consistent models

Models based on experimental measurements uses voltage, current (total, ion, electron), impedance, electron density, electron temperature, ion flux, excited or ground-state densities of species, consumption of gas precursors, deposition rate, etc. as model inputs. These models further analyze and interpret experimental measurements allowing conclusions for quantities not directly measurable [41].

Self-consistent models have the advantage that can be applied to any system if a specific geometry is given and they handle all sub-processes.

According to the mathematical approach of the solution, self-consistent models can be further classified as the following [41] [42]:

- Analytical models
- Numerical models

Analytical models are usually based on a higher number of assumptions. They are used mostly for one dimensional simulations and almost exclusively for the modeling of the plasma electrical properties. The most common approach in these models is to separate the discharges in three regions as two sheaths and the bulk plasma [41]. It is the easiest and the fastest way to simulate electrical properties of discharges and in some cases have lead to excellent results. However, the implementation of this kind of models to the rather complicated molecular gas discharges and their use is limited to the simulation of noble gas discharges [42].

Numerical models are generally more popular in self-consistent plasma modeling. They can be further distinguished, according to the methodology used for the management of electron and ion transport in RF discharges, in the following categories:

- Kinetic Models
- Fluid Models
- Hybrid Kinetic/Fluid Models

Kinetic models are time and spatially dependent solutions of the Boltzmann equation which produces electron and ion velocity distributions either by direct integration of the equation or by applying statistical techniques [41].

Fluid models solve moments of the Boltzmann equation in time and space, while the electron energy distribution function is calculated off-line and coupled to the fluid model providing the electron transport coefficients and the rate of electron molecule reactions. The fluid approach is not so accurate compared to kinetic methods, however it has shorter computational times [41].

Hybrid models use the kinetic approach in order to handle the non-local transport of electrons and ions in the discharges and to derive transport coefficients of charged species. The fluid approach is simultaneously applied in order to provide the density of the electron and ion and the electric field distribution [36]. Hybrid models have been developed in order to simulate rather complexities [41]. The transport coefficients and the rate of reactions of electrons with molecules are derived kinetically, while the density of species and the time and space variation of the electric field are calculated using the fluid flow approach.

Nowadays, hybrid models are implemented very often especially in plasma-based applications since they combine the accuracy of kinetic models with the high dimensionality and short computational times of fluid models [41].

3.2 Plasma Modeling Codes

Laser produced plasma parameters such as electron and ion temperatures, electron and ion densities can be modeled by hydrodynamic codes. EHYBRID (Pert 1983), LASNEX (Zimmerman et al. 1975, Young et al. 1997), MEDUSA (Christiansen et al. 1974, Djaoui and Rose 1992), ICF3D (Shestakov et al. 2000) can be mentioned as the hydrodynamic codes [37].

In order to calculate temperature and density of the particles of a laser produced plasma, the fluid equations should be solved. These equations can be solved by a well-developed algorithm. There are two approaches to solve them, namely, Eularian and Lagrangian methods (Figure 23). In both approaches, plasma can be thought as a box which is separated into small cells.

Eularian method keeps the volume of these cells of the box constant and assumes particles moves through the cells since plasma is expanding. This change in number of particles in a cell results in change of the density of it. However, in Lagrangian method, number of particles in a cell is thought to be fixed. This time, the cell gets larger or becomes compressed to keep the number of the particles constant and this altering in the volume of the cell leads change in density [43]. It is relatively easy to compare Lagrangian models with experiments, as each particle in the simulation correspond to one particle in the experiment [44].

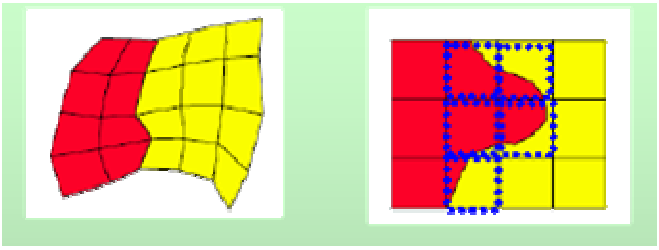

Figure 23 (a) Lagrangian approach, (b) Eularian approach [45].

3.2.1 Hydrodynamic Codes

ICF3D is a 3 dimensional code written in C++ programming language in order to model the high temperature plasmas. 1-D Lagrangian LASNEX is developed at LLNL (Lawrance Livermore National Laboratory). It calculates detailed numerical hydrodynamicals. Excited state-number density calculator MEDUSA, is improved at Rutherford Appleton Laboratory. It is also in Lagrangian form and one dimensional [37]. Another hydrodynamic code, EHYBRID, developed at York which is an extensive and successful in the prediction of experimental observables will be discussed in Section 3.3.

3.2.2 Raytrace Codes

To obtain a clear understanding of the output of a collisionally-pumped laser, raytracing is necessary to ascertain affects of refraction, how effectively the gain regions can be sampled before the laser beam is refracted out of the plasma. So the hydrodynamic codes are coupled to raytracing post-processors which model the transport of the x-ray laser along the extended plasma column. RAYTRACE (Plowes et al. 1996, King et al. 2000) (detailed in Section 3.3) and B3DRTX (Temporal et al. 2001) are the examples for raytracing [37].

3.2.3 Collisional Radiative Codes

The collisional radiative model (CRM) is capable of including most important atomic processes, such as collisional excitation, ionization, photoionization, radiative and dielectronic recombination [37]. It is also possible to choose a subset of the processes to investigate the effects of the non-mentioned ones. The model uses an efficient iterative procedure to solve the statistical balance. Since the method can include all atomic processes; it can be used to investigate various density effects [46]. The atomic data for CR modeling was generated by the HULLAC suite of computer codes [47] and it is used in hydrodynamic codes as post-processor.

3.3 Method of Simulation: EHYBRID

EHYBRID is a 1.5D hydrodynamic / atomic code developed at the University of York by Geoff J. Pert with help from a number of graduate students over the years [48]. The aim of the code is to model the detailed interactions in a high temperature laser produced plasma to calculate the lasing on x-ray lines in, for example, Ni-like and Ne-like systems [21].

EHYBRID, which was developed to understand the evolution of the lasing material, describes many physical processes, including pump laser energy

deposition, hydrodynamic motion, electronic thermal conduction, ion-electron thermalisation coupled with the atomic physics of the lasant ions [23]. The model is 1.5-dimensional or quasi-2 dimensional [23], designated to operate in planar geometry [21]. The code calculates, at each time step and for each cell, electron temperatures and densities, ionic fractions from neutral to bare nuclei, and, using a detailed set of collisional-radiative equations, atomic level populations of the interesting Ne, F, Co and Ni- like ions [24]. The code uses a 98 Lagrangian cell matrix in the direction away from the target. The fluid is hence modeled in the direction parallel to the driving laser by cells, which are assumed to be laterally isothermal, and, as such, the transverse expansion is considered to be self-similar [21]. Such approximations have been described in detail elsewhere (Pert 1979, 1983 [48]).

The calculation of the ionization balance within the plasma, and in particular the abundances of the Ni-like, Na-like, Ne- and F-like ions are of central importance in these simulations.

3.3.1 Main Program and Post-Processors

In the direction towards the laser, the main program solves the fluid equation of continuity and the Navier–Stokes equation to calculate the density profile. Energy transport in the direction parallel to the laser is reduced from the free streaming limit by a flux limiter of 0.1. The program evaluates inverse bremsstrahlung absorption, with resonance and other critical density absorption taken into account by dumping 30% of the input laser energy at the critical density. The code does not explicitly model other laser absorption mechanisms. One third of the experimental laser energy in order to allow for un-modeled laser interaction processes such as laser scatter [49].

The collisional radiative process which is the sub-program (or post processor), models to calculate the Ne- and F-like populations include collisional and

radiative excitation/de-excitation, collisional ionization, radiative recombination, three body and di-electronic recombination.

To fully compare simulation with experiment the output of the Lagrangian code is coupled to a raytracing post-processor which models the transport of the x-ray laser along the extended plasma column [40]. The refraction calculation is performed with a 2D raytracing model derived from the work of Toft (1979) which traces ~10^5 angular bunches of rays through the plasma, accounting for spontaneous emission and amplification [50]. A general description of these codes can be found in Holden et al [23].

The ray-trace program derives from well tested routines designed to model the absorption of the driving laser by the plasma. The plasma variables are defined on a rectangular grid, each cell of which is divided into two triangular cells for the purposes of ray-tracing. The refractive index gradients within the cells are assumed constant, defined by the densities at the cell corners. In uniform refractive index gradients, ray paths are parabolic and the total ray path is calculated as a smooth sequence of parabolic arcs between the cell faces [23]. The raytracing code takes into account effects due to refraction and saturation and can operate in a traveling irradiation wave geometry of v = c or ~ ∞, where v is the velocity of the traveling wave [40].

3.3.2 Manipulation of EHYBRID (Input-Output)

The input parameters for EHYBRID are the full width at half maximum (FWHM) of the pulse duration, the power of the laser pulse, and all of the three dimensions of the target and a file containing the atomic data of the lasing material. Atomic data are calculated using the code developed by Cowan [51].

The outputs of the code are various calculated plasma parameters such as electron temperature, density, gain, ionization given as a function of cell position and time. The resonance and lasing lines can also be gathered from the code.

3.3.3 EHYBRID in Literature

EHYBRID code uses not only atomic data from Cowan, but also some other data could be added. In Holden et al. [50] the Ne-like Fe ion with 38 excited levels, including the $2s^2 2p^5 3s$, $2s^2 2p^5 3p$, $2s^2 2p^5 3d$, $2s^2 p^6 3s$, $2s^2 2p^6 3p$ and $2s^2 2p^6 3d$ configurations is fully modeled, using multiconfigurational Dirac–Fock (MCDF) atomic data (Grant et al 1980) [50].

The code can calculate F-like, Na-like, Ne-like, Ni-like ion levels. For instance, the populations of 12 levels of the Na-like ion, 113 levels of the Ne-like ion and 216 levels of the F-like ion are explicitly modeled in Demir et al. [24]. The atomic physics input file for Ag was constructed at LSAI, in Orsay. The Ni-like ion stage is modeled with 272 excited levels including all levels in the n=4 and 5 manifolds and with averaged contributions from the n = 6 to 8 levels [40].

EHYBRID could cooperatively used with other codes. The complex problem of a collisionally pumped Ne-like germanium laser is examined through several detailed models. EHYBRID is used for the central model at Holden et al. [23], which self consistently treats the plasma expansion with the atomic physics of the Ne-like ion for 124 excited levels through a collisional radiative treatment [23].

In many previous studies it is demonstrated that EHYBRID gives excellent agreement to experimental results, which improves the reliability of the code. For example, in a study from Raymond et al. [40] for the Ni-like Ag laser the theoretical foresight was very much similar to the experiment performed. The Ne-like and Fe-like iron plasma-based x-ray laser experiment was simulated with EHYBRID correctly by Demir et al. [24].

CHAPTER 4

PROPOSED EXPERIMENTAL SETUP DESIGN AND THEORETICAL INVESTIGATION FOR LASER PRODUCED Ni-LIKE Sn PLASMA

4.1. Proposed Experimental Setup Design

Time- and space-resolved spectroscopic analyses for estimating the spectrum; therefore ionization degree, electron temperature and density of the nickel-like tin plasma can be performed by irradiating it with a Nd:YAG laser (CFR 400 BIG SKY LASER) operated at 10Hz. This laser works at 532 nm, the second harmonic generation, with 6ns of pulse duration (or FWHM for a Gaussian-fit profile). A proposed experimental setup with the laser and related equipment is given in Figure 24. The laser power reaches 3.83×10^7 W for a pump-pulse energy of 230 mJ. The laser beam can be focused onto the target surface at normal incidence using an f /12 antireflection-coated planoconvex lens. This lens and the 1.0 mm tin target at high purity (99.99+ %) need to be placed inside a vacuum chamber which is obligatory for an x-ray analysis. A stainless-steel vacuum chamber with radius 500 mm and height 750 mm can be pumped using turbo pump (Varian 551 TV navigator) to achieve $\sim 10^{-5}$ Torr.

Fiber optic receiver connected to a high resolution spectrometer (Ocean optics S2000 fiber optic, HR4000 High-resolution spectrometer) is capable to detect the visible region spectrum. In order to record x-ray emission spectrum a back-illuminated x-ray charge-coupled device (CCD) camera (Andor's DX420) connected to a computer is necessary. It can be placed inside a vacuum chamber to minimize the distance between the source and the detector. In order to avoid

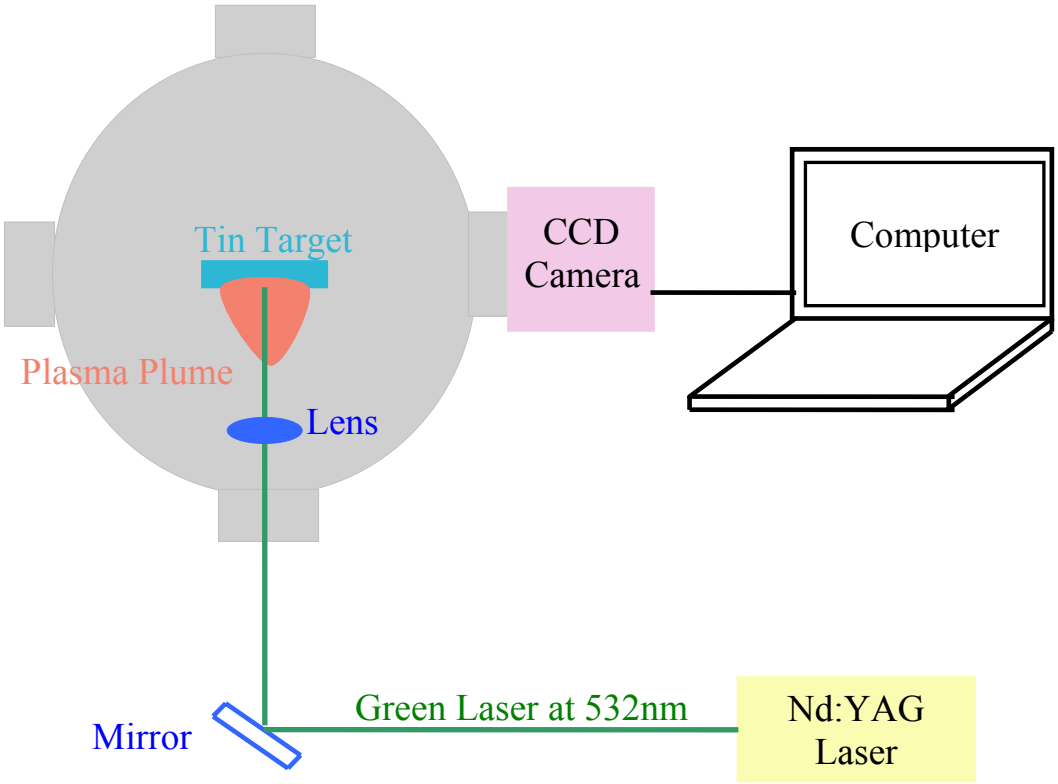

Figure 24 Schematic of the experimental setup used for emission spectroscopic studies

saturation of the sensitivity of the CCD for the 12.0 nm line, the second-order light of the x-ray laser at 24.0 nm can be used.

4.2. Theoretical Investigation for Laser Produced Ni-like Sn Plasma

A computer simulation code which is verified with an experiment is the most reliable code to use. There have been many research groups who have verified EHYBRID with experiments. Besides, an experiment in excellent agreement with a code has many advantageous research fields. By the means of the EHYBRID, the experiment can be investigated in various ways. Emission lines, ionization degree, gain, electron temperature and density can be discussed with the output of the code; when power or intensity, wavelength and FWHM of the pumping laser pulses are given as input to the code.

The laser produced plasma of tin is composed of Co-like and mostly Ni-like ions. Spectrum data from EHYBRID code is analyzed for Ni-like and Co-like resonance lines of the tin target. The lines are labeled as in the Figure 25. Although the power of the pumping laser of the plot (b) differs from the plot (a) with ~10^7, the photon intensities differs only order of tens. The given pumping powers for the Figure 25 are 2.83×10^7 W and 3.83×10^7 W, respectively.

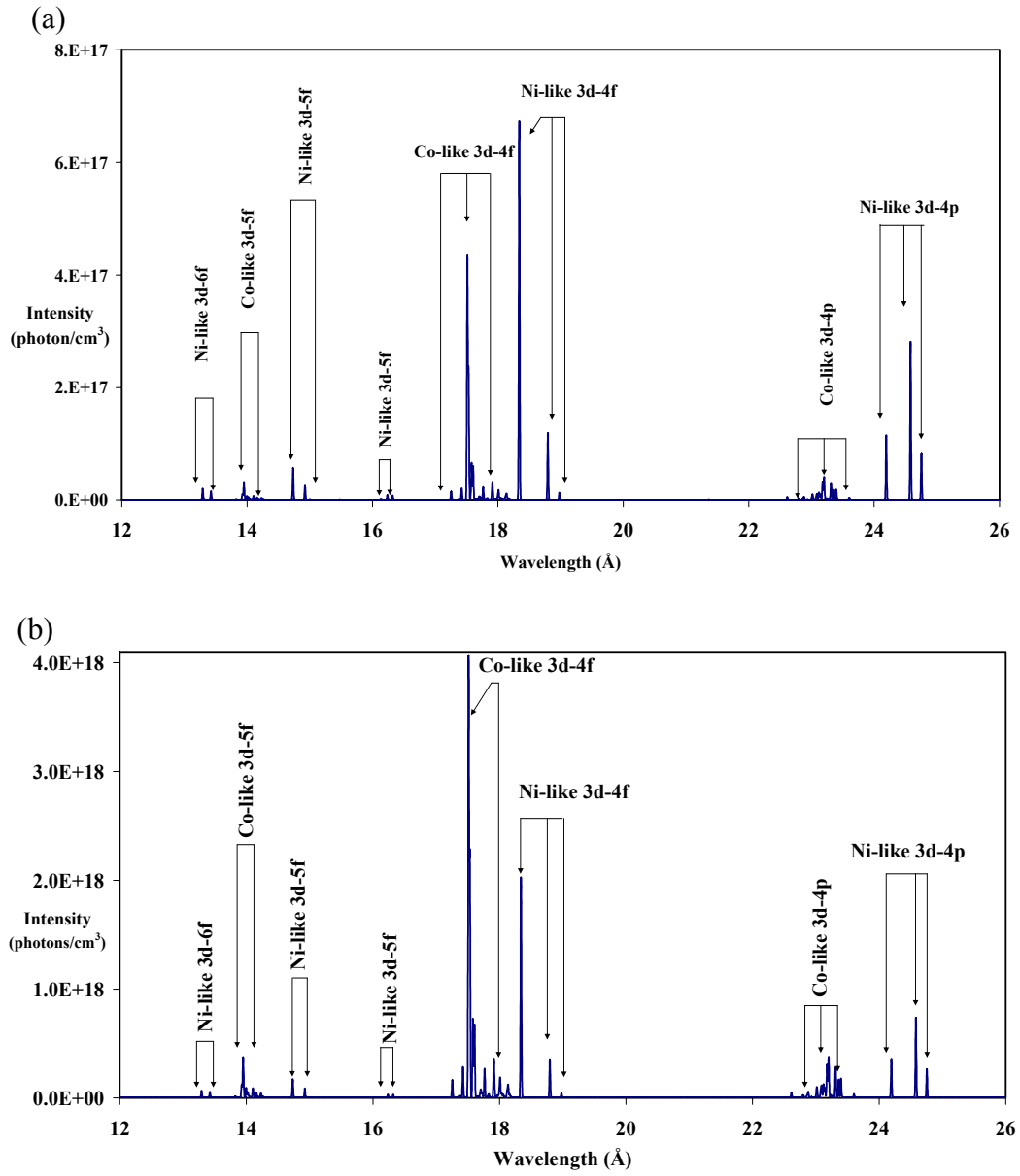

Figure 25 Calculated resonance lines emitted from Sn plasma (pumping power of 2.83×10^7 W and 3.83×10^7 W, respectively)

FWHM (Full width at half maximum) value is used to investigate the x-ray emitted from the slab tin target by the means of the resonance lines. For having large population inversion closed shell ions are preferred as stated at Section 2.3.3.

In Figure 26, Co-like and Ni-like resonance lines are calculated by a graph of photon number per time step versus time. The two resonance lines are summed to have a total FWHM parameter to compare with different inputs. In plot (a) and (b) of Figure 26, the power of the pumping laser is 2.83×10^7 W, but the spot diameter is altered from 50 µm to 30 µm which alters the intensity from 1.44×10^{12} W/cm^2 to 4.00×10^{12} W/cm^2 .Spot size can change by using a focusing lens experimentally. In plot (c) and (d) the spot diameter changes from 50µm to 30µm while again the pumping laser is kept constant, but this time at 3.83×10^7 W, that makes intensities change from 5.42×10^{12} W/cm^2 to 1.95×10^{12} W/cm^2. The broader is the FWHM, the bigger is the x-ray possibility. That implies the fourth plot with the highest pumping power and the lowest spot diameter is the more suitable candidate to obtain x-ray with ionizing more electrons from tin target.

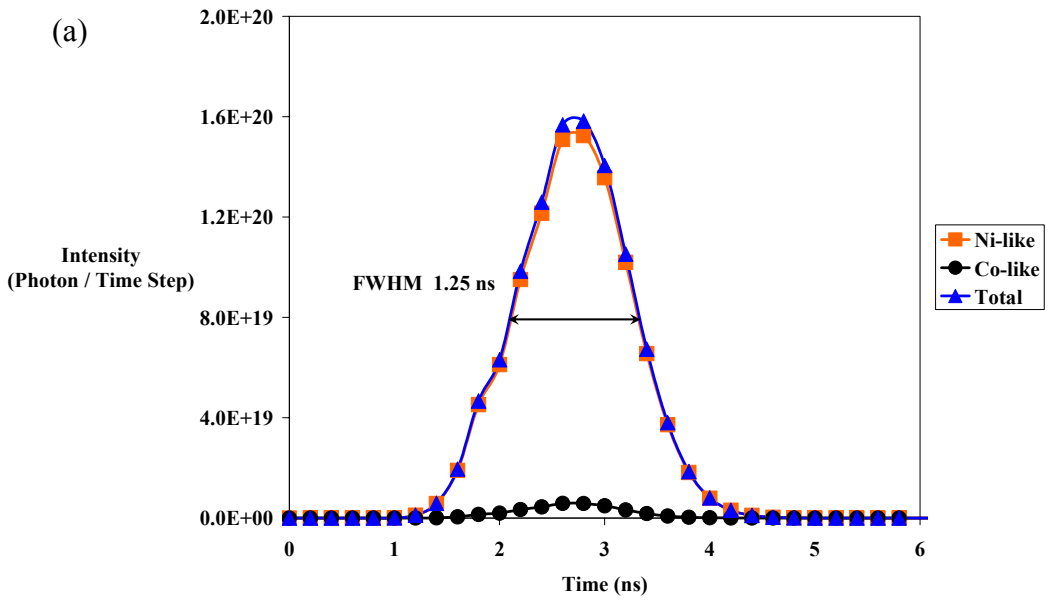

(b)

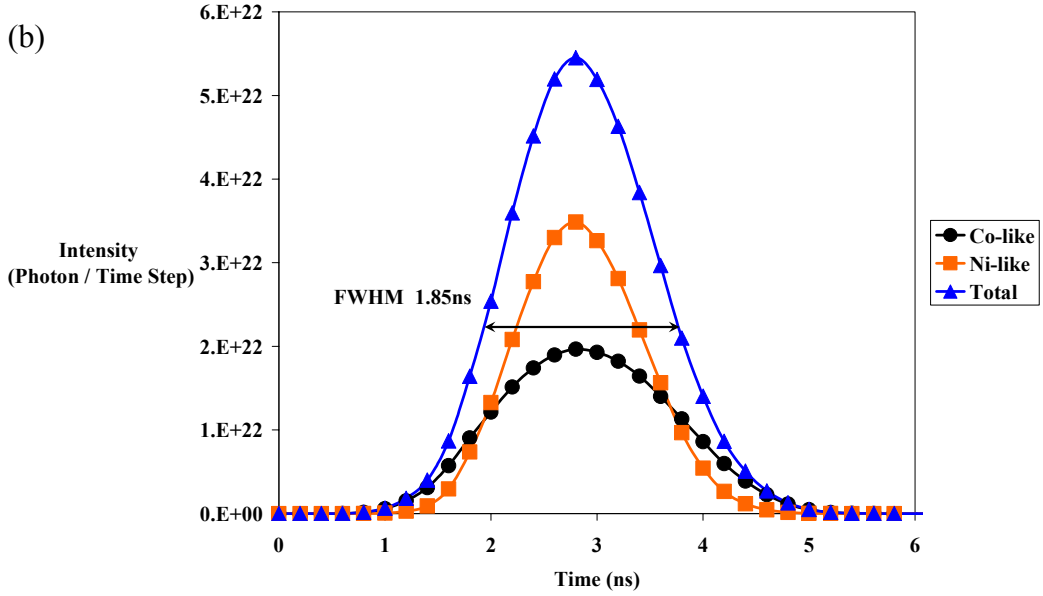
6.E+22
5.E+22
4.E+22
3.E+22
2.E+22
1.E+22
0.E+00
Intensity
(Photon / Time Step)
FWHM 1.85ns
0
1
2
3
4
5
6
Time (ns)
Co-like
Ni-like
Total

(c)

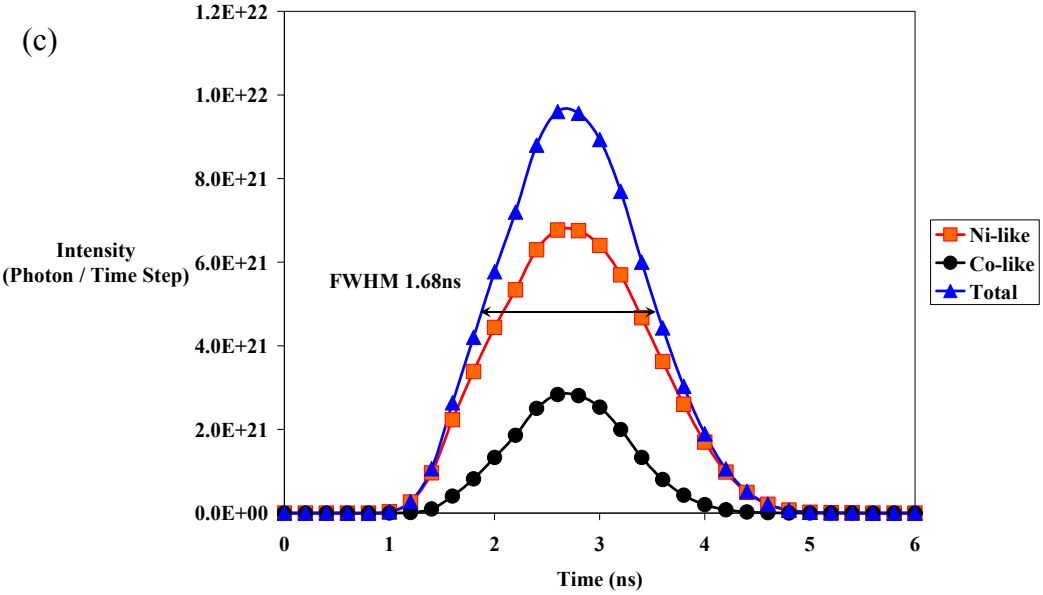
1.2E+22
1.0E+22
8.0E+21
6.0E+21
4.0E+21
2.0E+21
0.0E+00
Intensity
(Photon / Time Step)
FWHM 1.68ns
0
1
2
3
4
5
6
Time (ns)
Ni-like
Co-like
Total

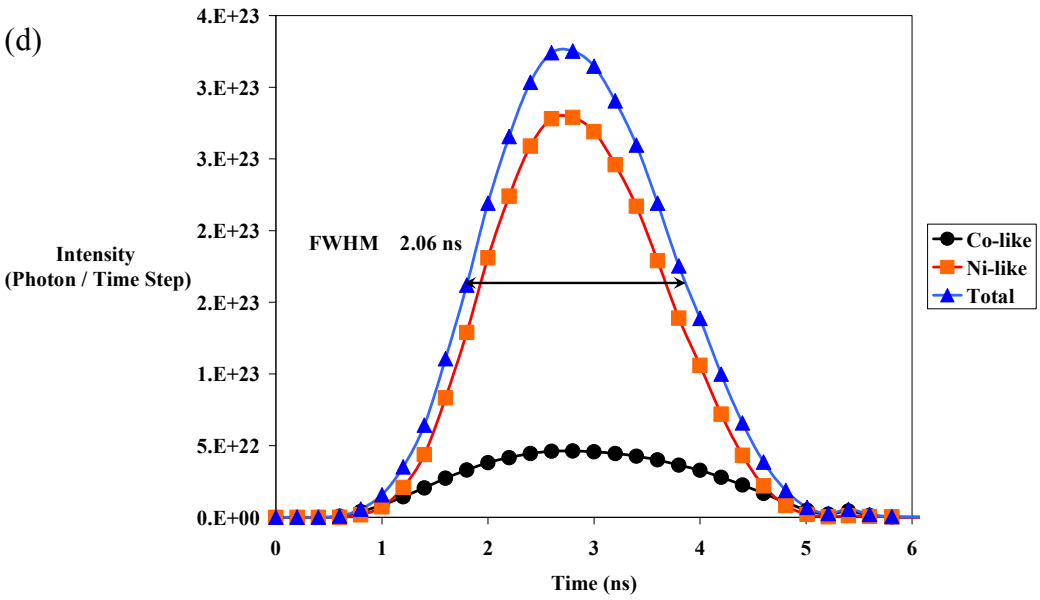

Figure 26 FWHM of Ni-like, Co-like, and total resonance lines intensity as a function of time for different laser pumping pulse intensities, pumping laser intensities are (a) 1.44 x10^{12} W/cm^2, (b) 4.00 x10^{12} W/cm^2, (c) 1.95 x10^{12} W/cm^2, (d) 5.42 x10^{12} W/cm^2

X-ray region is usually used for the wavelength region from 35 Å to 500 Å. When a target is irradiated with a laser, a wide range of spectrum can be detected. By means of intense lasers, x-ray region can also be detected and in order to have x-ray lasing the target should be at relatively stable state than an ordinary ion. This stable state results in population inversion and obviously in lasing. That situation can be reached by a closed shell-like ion formation. In our experiment, the target, tin, has 50 electrons and 22 of them should be removed to make it resemble to nickel. In the following Figure 27, the electrons that can be ionized for two cases are shown. The Nd: YAG laser pulse at 532 nm is focused onto the tin target at intensities 4.00x10^{12} W/cm^2 and 5.42x10^{12} W/cm^2, respectively. In plot (a) of Figure 27, about 21 electrons are ionized where in plot (b), the required number of electrons are removed from the target. Although x-ray emission can be detected in both cases, (Figure 25) x-ray lasing is a possibility only in the second case. The graphs in Figure 27 are drawn for the highest ionization degree of the cell of the EHBRID code which divides the target and plasma plume into 98 cells.

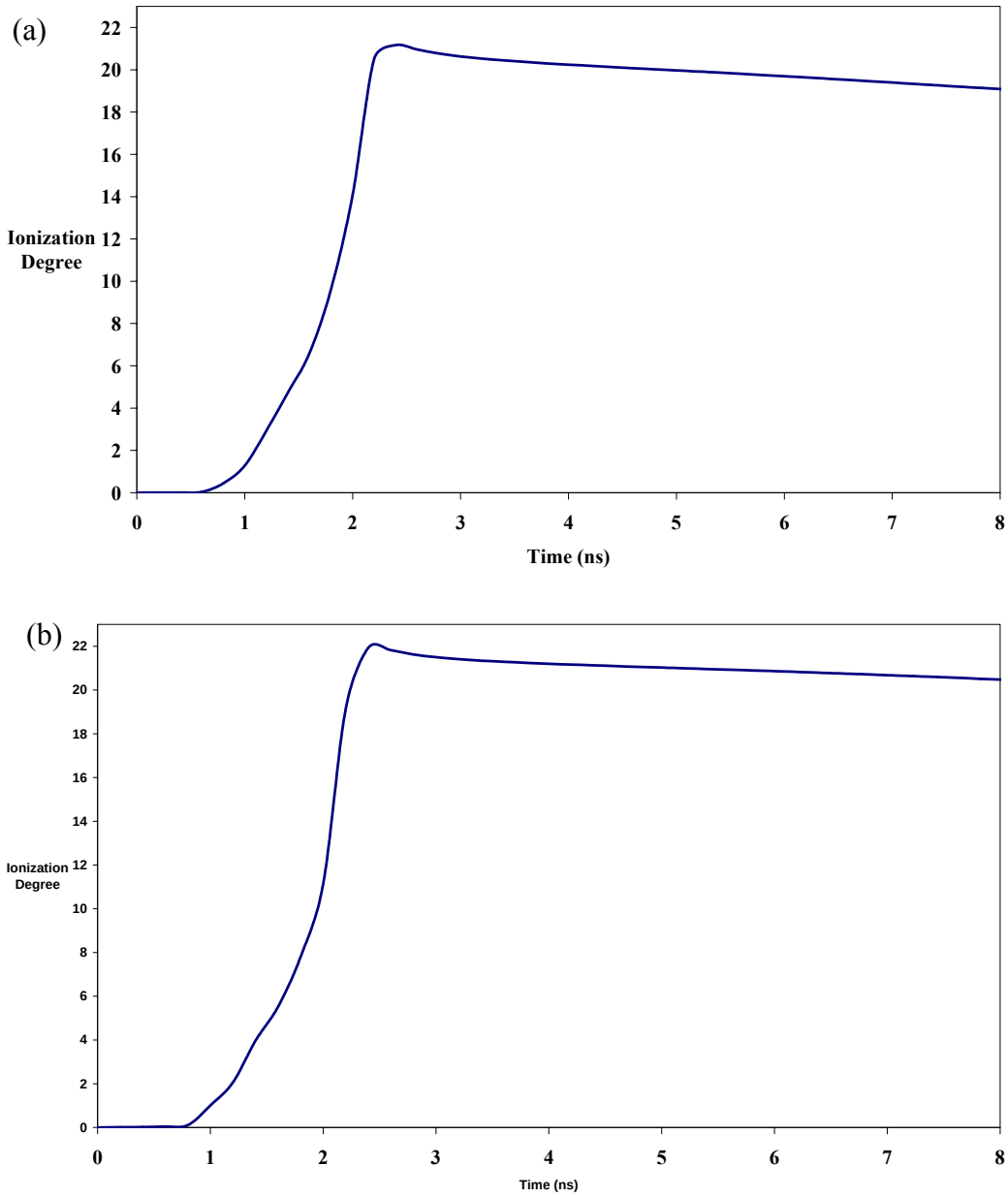

Figure 27 Electrons removed from the tin target versus time graph for intensities 4.00×10^{12} W/cm^2 and 5.42×10^{12} W/cm^2, respectively.

Ionization degree can be evaluated as linearly proportional to electron temperature and density in a sense. If the electron temperature is not high enough, the potential to remove electron from the target will be less or when electron density is not so huge, there will be small number of removed electrons. Change in electron temperature during the pumping process is shown in Figure 28.

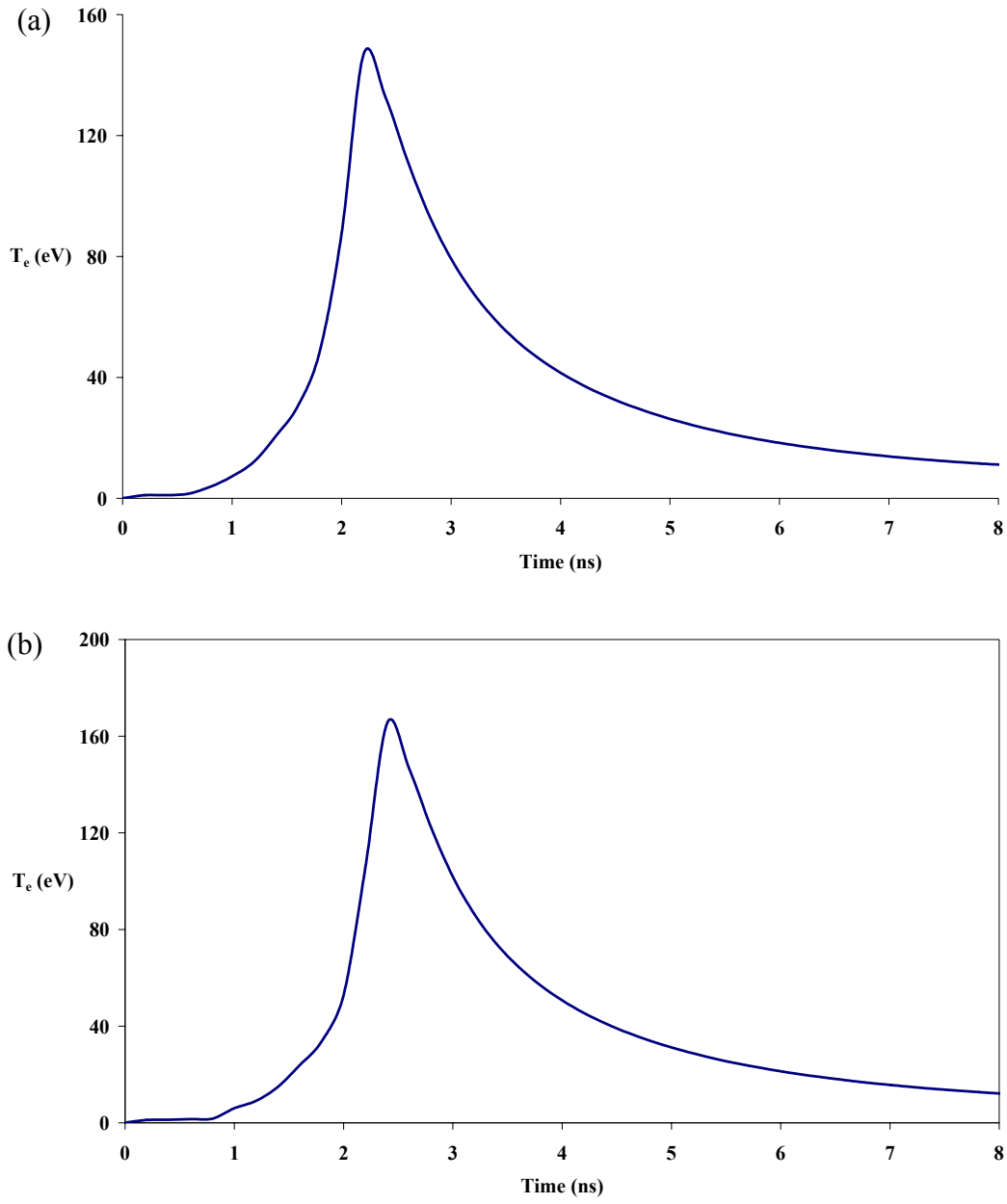

Figure 28 Temperature versus time for intensities 4.00×10^{12} W/cm^2 and 5.42×10^{12} W/cm^2, respectively.

As expected, electron temperature increases with pumping intensity, so does electron density (Figure 29). The graphs for both electron temperature and density are drawn for the cells with maxima.

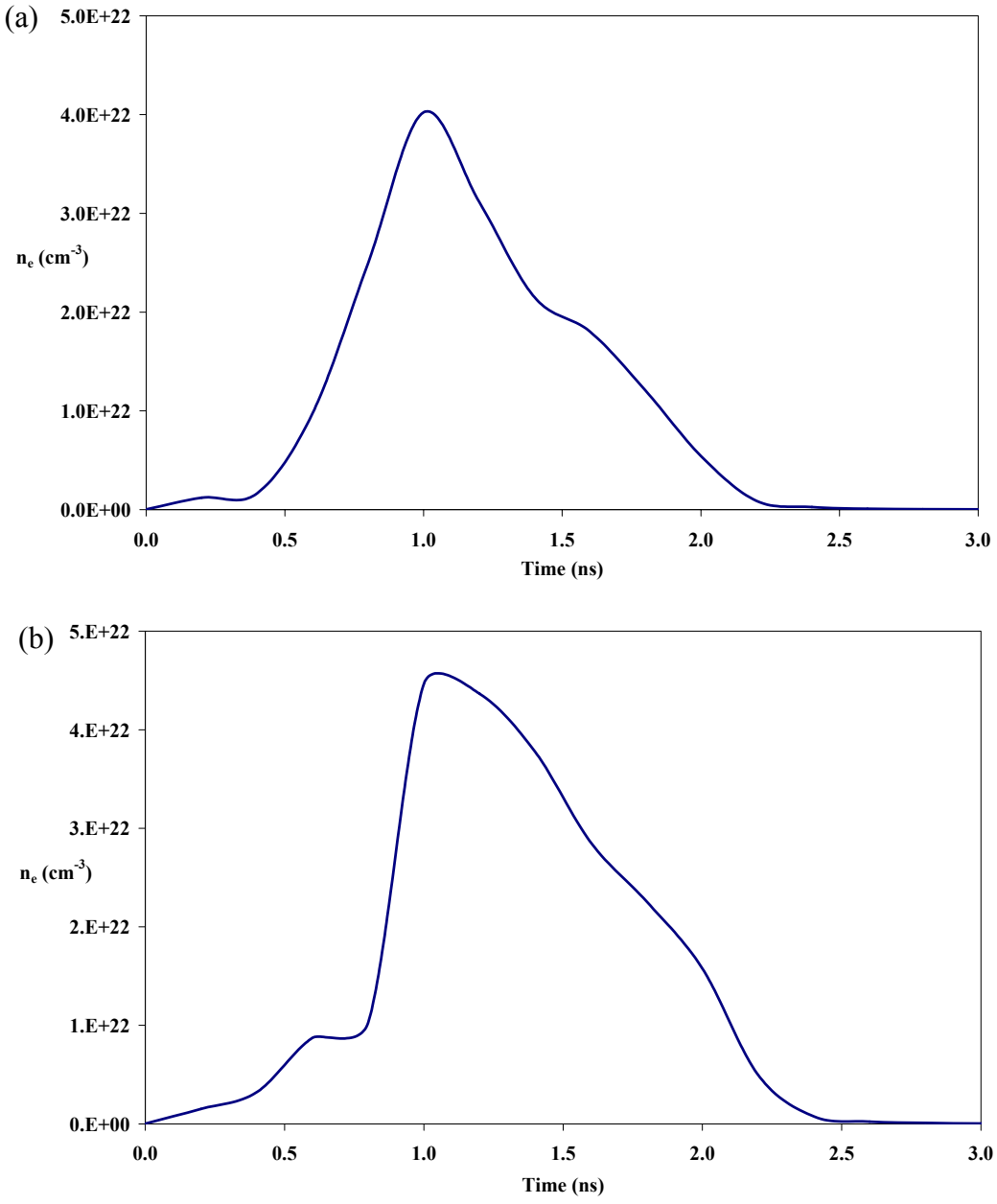

Figure 29 Electron density versus time graphs for intensities 4.00×10^{12} W/cm^2 and 5.42×10^{12} W/cm^2, respectively.

The lasing for Sn plasma occurs between 100 Å and 150 Å. The lines that the code predicts for the region are given in Figure 30 for the cases stated above. The plot (b) of Figure 30 has higher x-ray emission intensity for Ni-like 4d-4p transition at 116.6 Å than that of plot (a). It was an expected result because the FWHM values, temperature and ionization degree versus time graphs imply that the second plot has more chance to create population inversion.

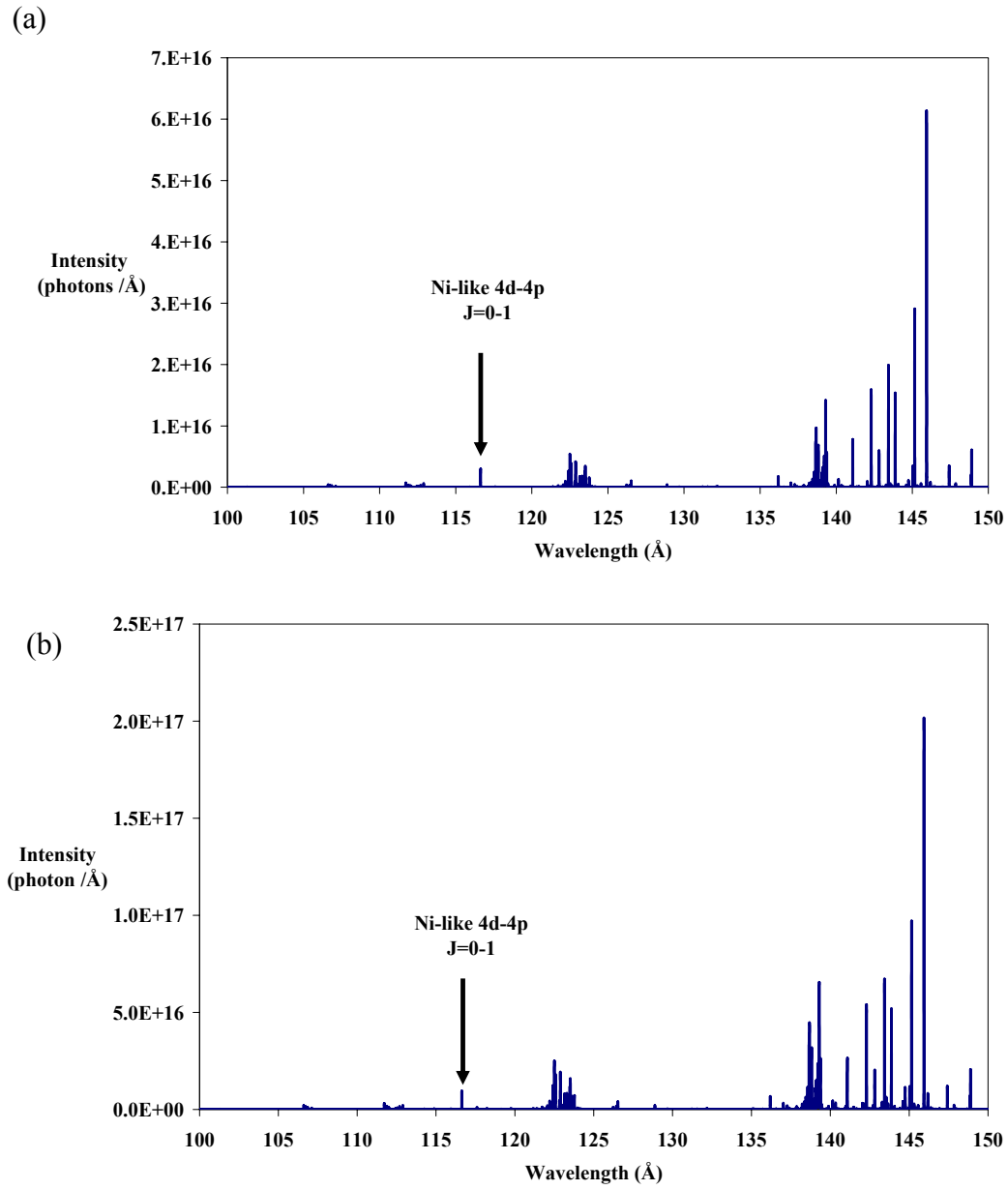

Figure 30 Transition lines for Sn between 100 Å and 150 Å

However, for both cases population inversion does not occur affectively, so gain is insignificant (Figure 32). The reason why the lasing does not come to the stage is that, the pumping laser is not intense enough. As discussed in Section 2.5, there are some other approaches for x-ray lasing. Gain for Ni-like 4d-4p transition at 116.6 Å can also be discussed by the means of the code. Gain graph for pumping intensity of 5.42×10^{12} W/cm^2 for 6 ns is drawn at Figure 31.

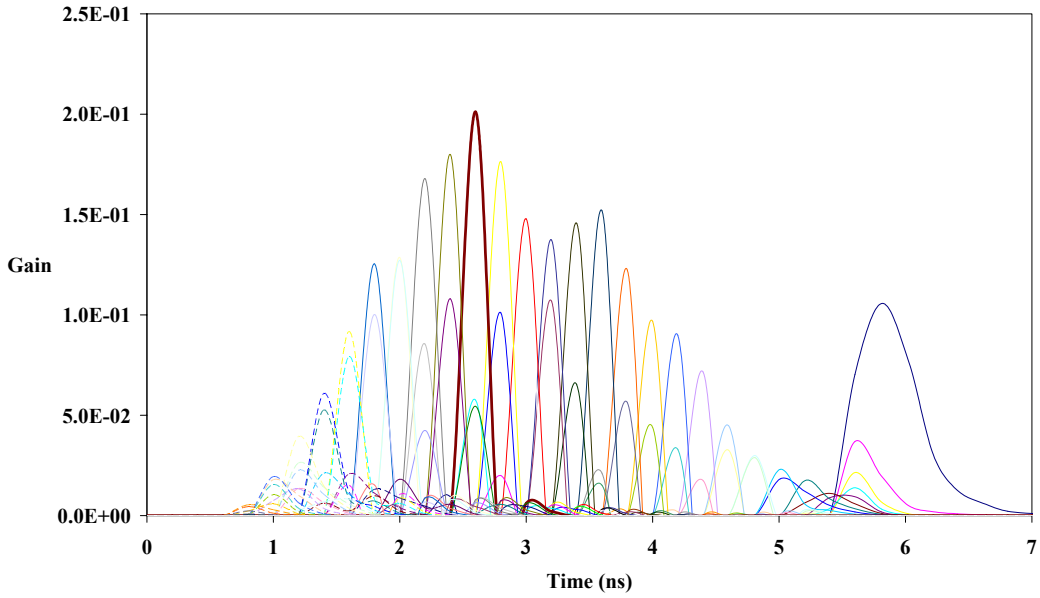

Figure 31 Gain versus time graph for pumping intensity of 5.42×10^{12} W/cm^2

Considering gain for all cells give an idea about the gain of the x-ray of a given situation, however discussing the cell with the highest gain is the real and common parameter. The cells with highest gain for the two different pumping intensities are given at Figure 32. In plots (a) and (b), improvement of gain with the increase in intensity can be seen.

Considering the changes in intensity, ionization degree, electron temperature, electron density and gain with respect to time enable investigating x-ray. Besides, the same investigation can also be issued according to their change with respect to distance of the plasma from the target (Figure 33, Figure 34 and Figure 35).

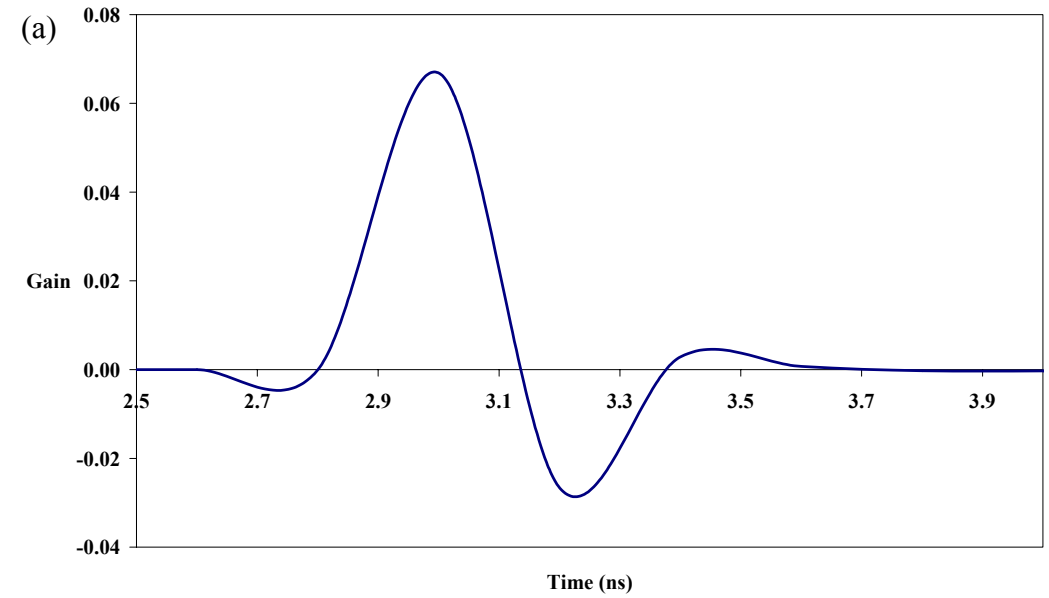

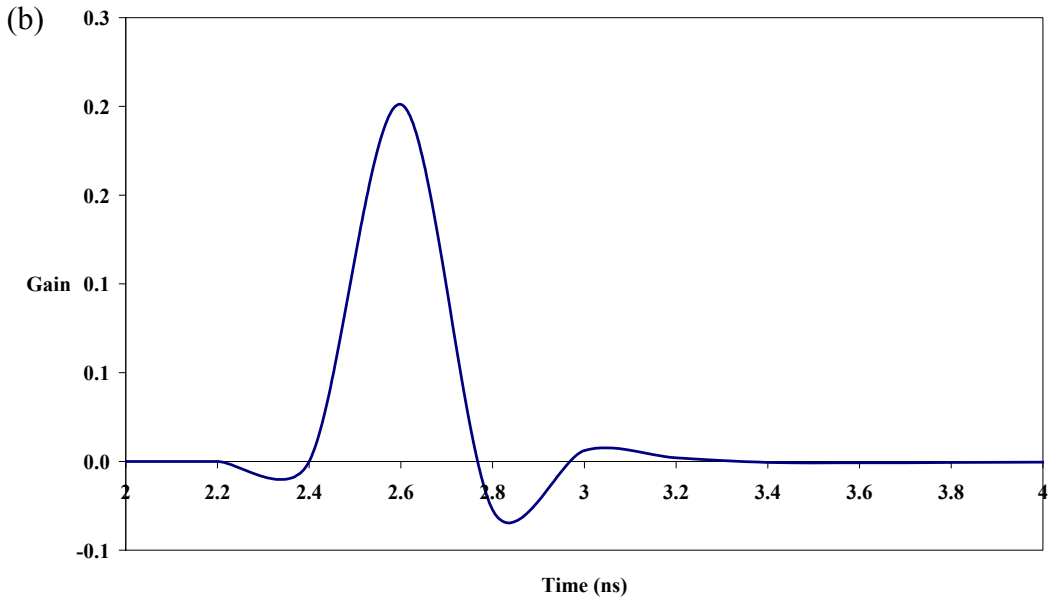

Figure 32 Graphs for the cell with highest gain versus time

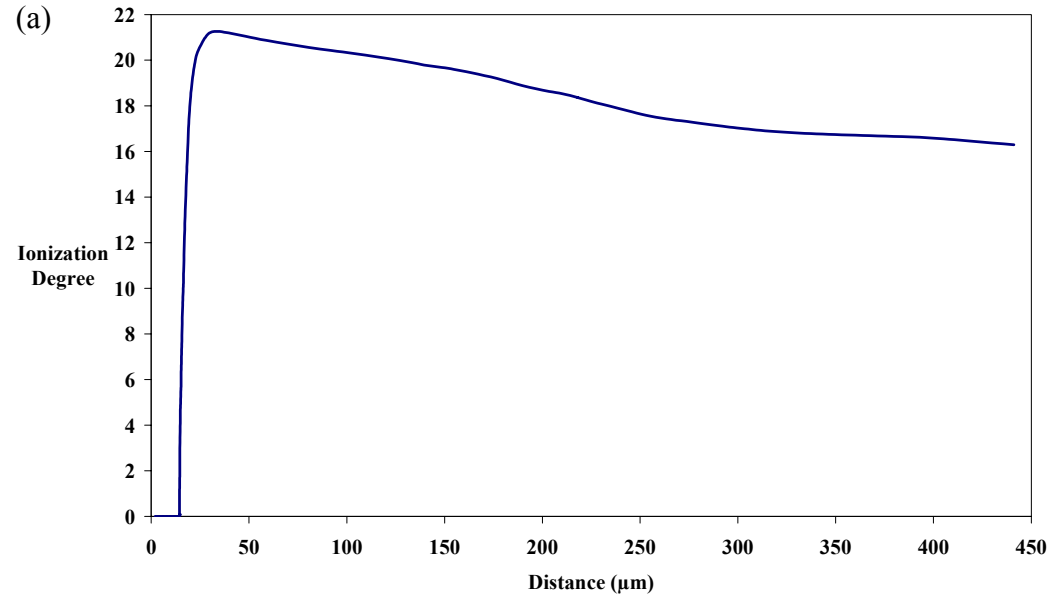

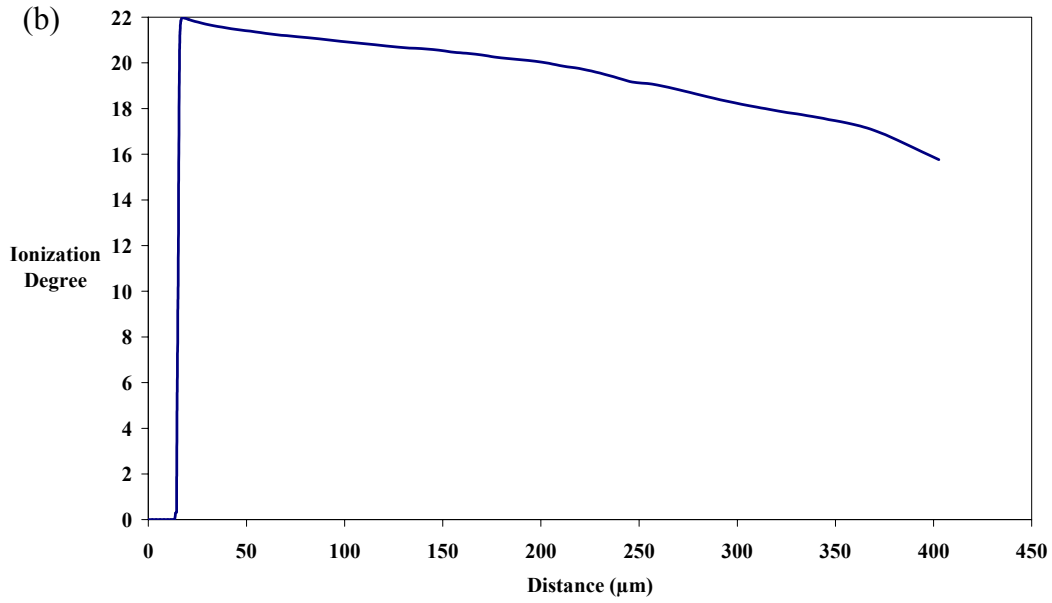

Figure 33 Ionization degree versus distance graphs for intensities 4.00×10^{12} W/cm^2 and 5.42×10^{12} W/cm^2, respectively.

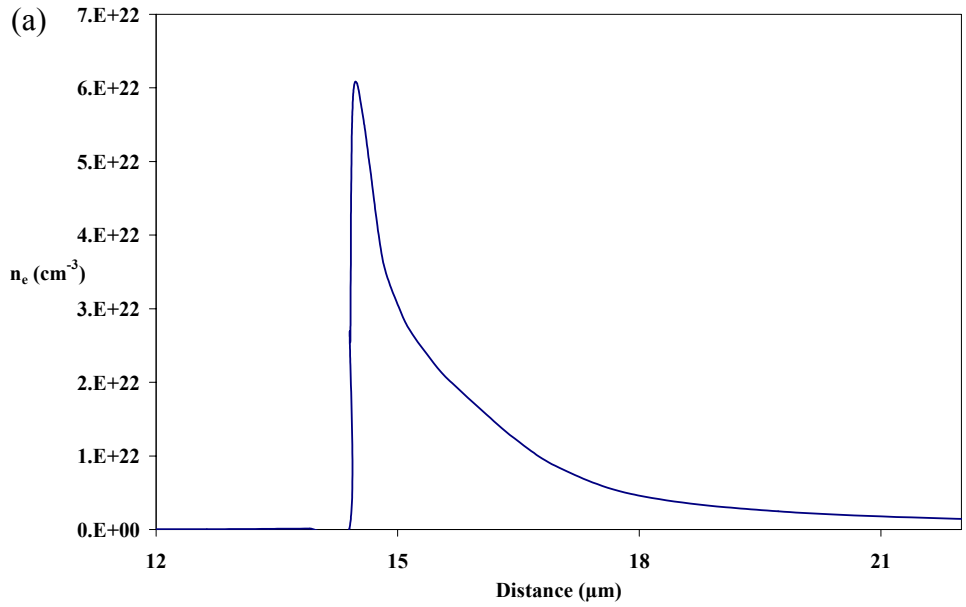

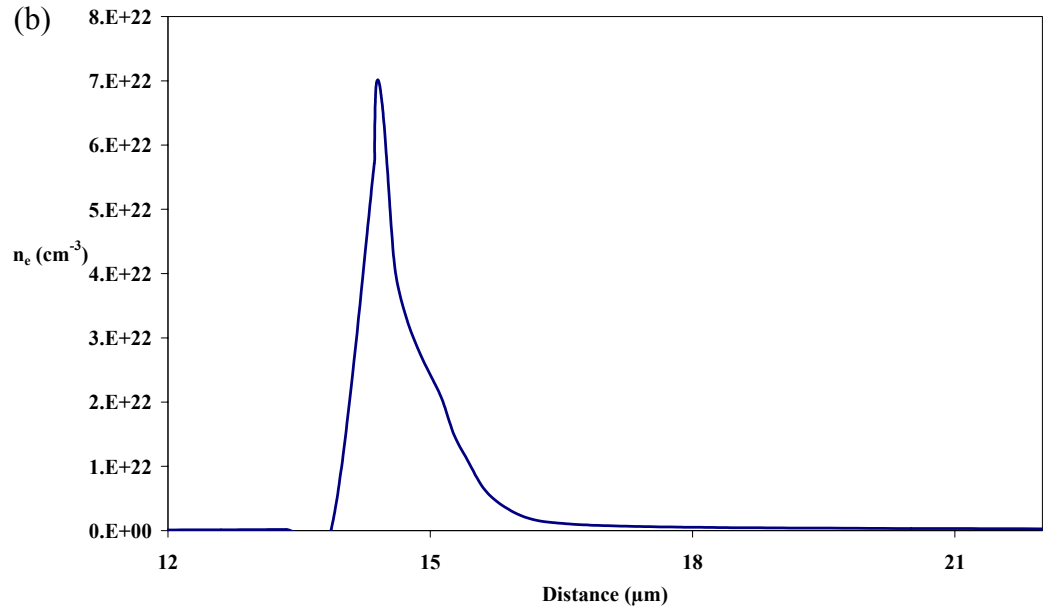

Figure 34 Electron density versus distance graphs for intensities 4.00×10^{12} W/cm^2 and 5.42×10^{12} W/cm^2, respectively.

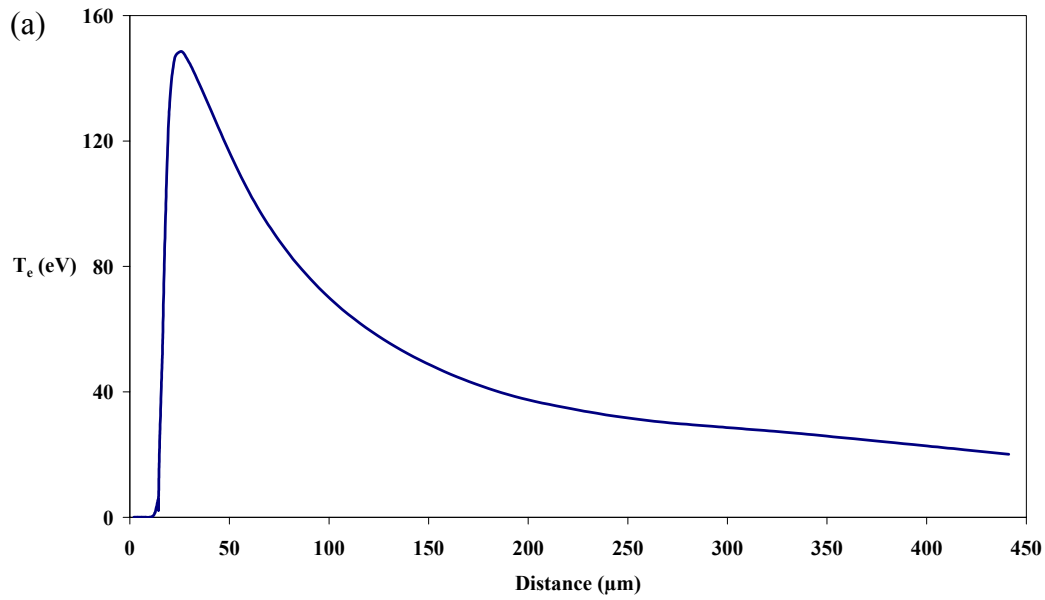

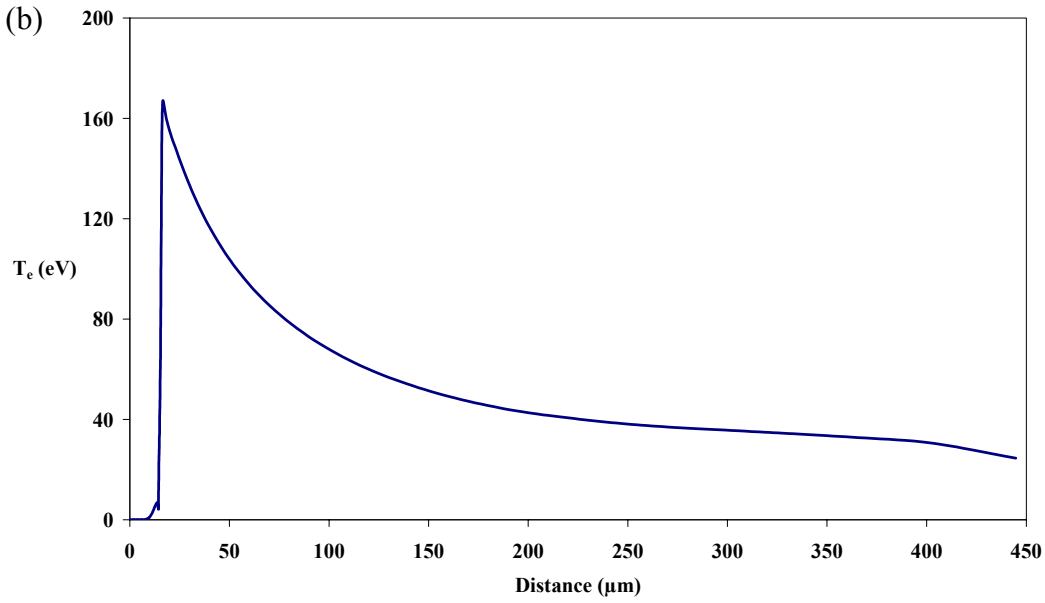

Figure 35 Electron temperature versus distance graphs for intensities 4.00×10^{12} W/cm^2 and 5.42×10^{12} W/cm^2, respectively.

All plots of Figures 33, 34 and 35 including distance of plasma plume showed that the maximum of the values occurs very near to the target. Since the plasma expands out of the target, the maxima are so close to it.

Ionization degree for the two cases can be studied with electron temperature and distance together (Figure 36). That will implies a rise in electron temperature will improve the ionization degree. White area in the plot (a) in Figure 36 is the region that is not reached by the code and that points it will not be reached during the experiment.

Gain can also be investigated with a contour plot to have idea of at what values for T_e the gain will be sufficient (Figure 37). The contour plot indicates that electron temperature should be raised rapidly to have effective gain value since the gain peaks at a distance close to the target, about 10 μm .

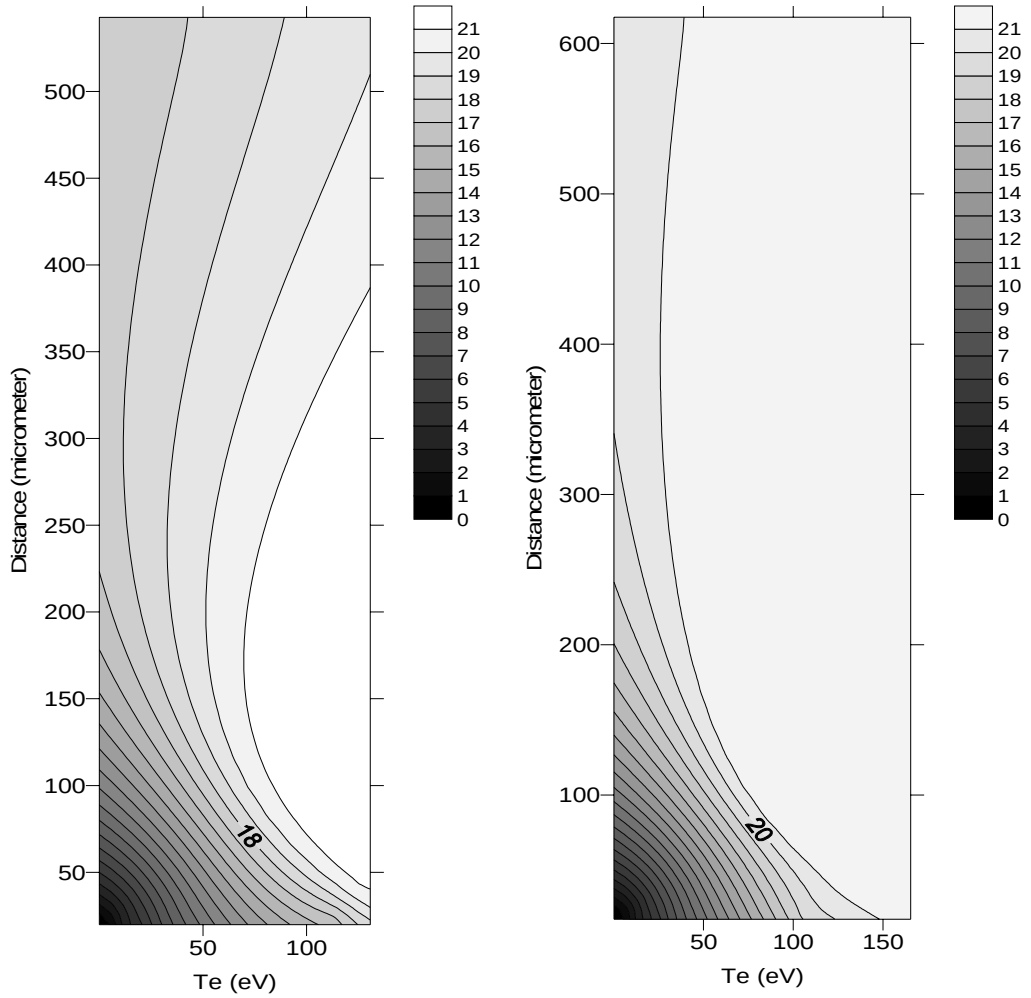

Figure 36 Ionization degree contour graphs for intensities 4.00×10^{12} W/cm^2 and 5.42×10^{12} W/cm^2, respectively.

Moreover, it is possible to draw a graph to consider the rise in gain with the rise in pumping intensity. Fixing all parameter including the spot size (30μm), gain can be investigated with respect to pumping power altering as $2.83x10^7$ W, $3.83\ x10^7$ W, $4.83\ x10^7$ W, $5.83\ x10^7$ W (Figure 38 (a)). Then the intensities are $4.00x10^{12}$ W/cm^2, $5.42x10^{12}$ W/cm^2, $6.83x10^{12}$ W/cm^2 and $8.25x10^{12}$ W/cm^2. It is obvious that, for a case that is not responsible for x-ray lasing, gain is directly proportional to intensity of the laser. Changing the laser power leads a change in intensity of the pumping laser and that results in a change in the gain. This time, keeping the pumping power constant ($3.83x10^7$ W), but varying the spot size (20 μm, 30 μm, 40 μm, 50 μm) will lead the change in gain (Figure 38 (b)). Therefore, the spot size is inversely proportional with gain, since it is also inversely proportional with pumping intensity.

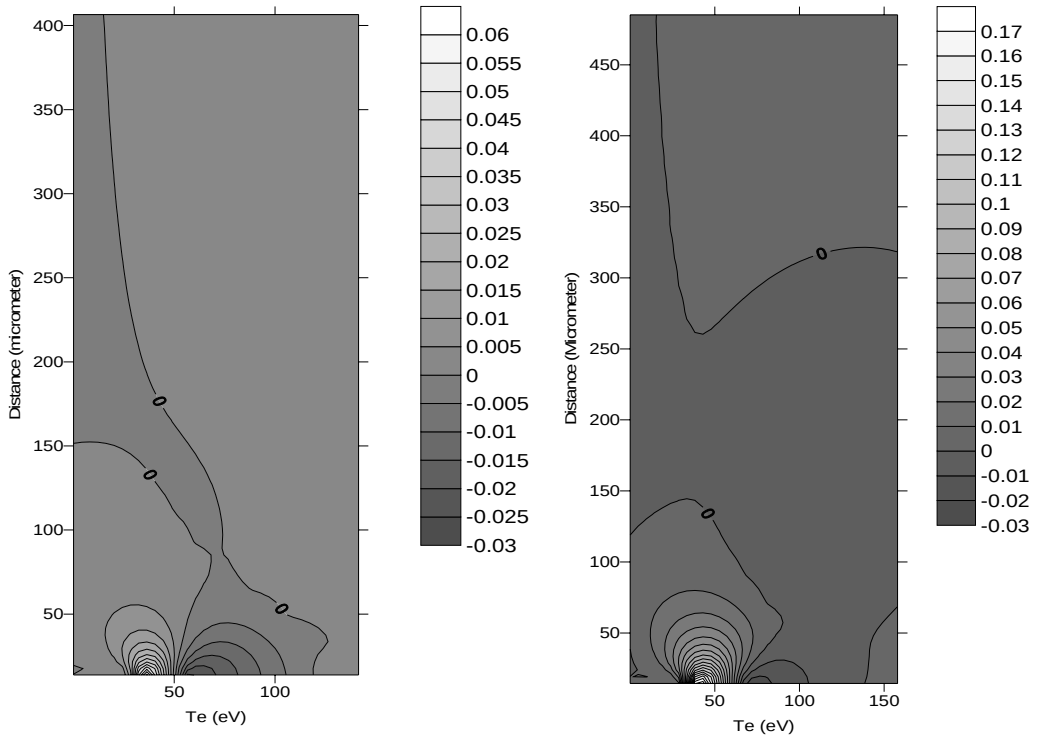

Figure 37 Gain contour graphs for intensities $4.00x10^{12}$ W/cm^2 and $5.42x10^{12}$ W/cm^2, respectively.

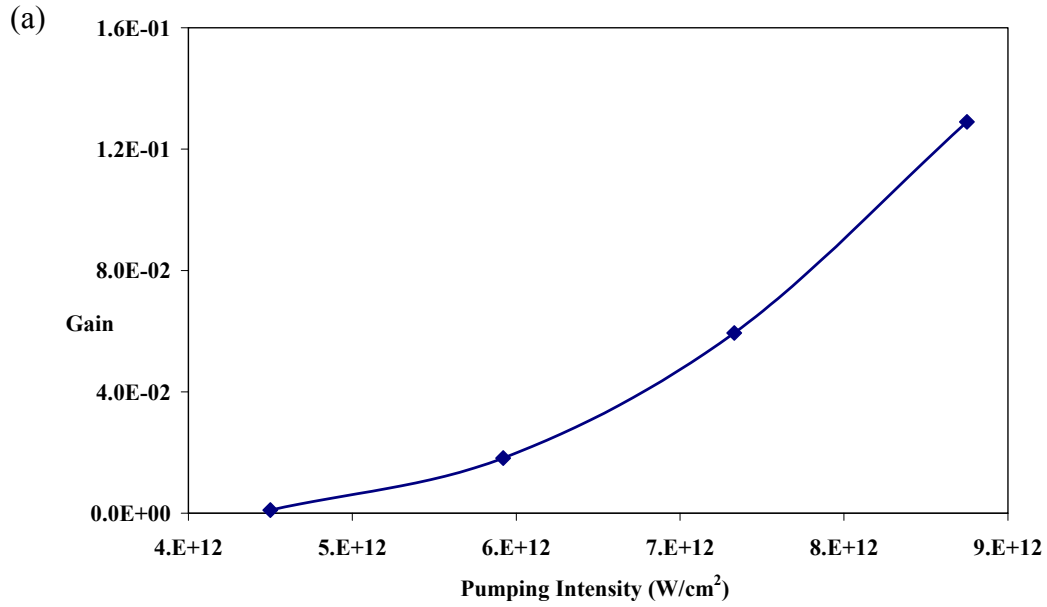

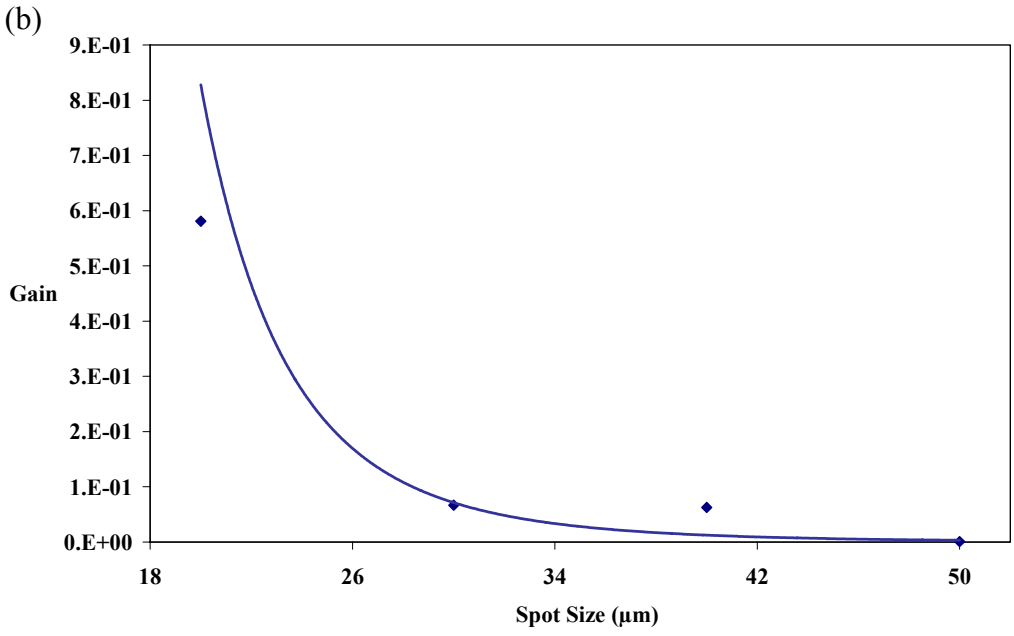

Figure 38 (a) Gain with intensities 4.00×10^{12} W/cm^2, 5.42×10^{12} W/cm^2, 6.83×10^{12} W/cm^2 and 8.25×10^{12} W/cm^2, (b) Gain with spot sizes 20 µm, 30 µm, 40 µm, 50 µm.

Moreover, it is possible to draw a graph to consider the rise in gain with the rise in pumping intensity. Fixing every parameter including the spot size (30 μm), gain can be altered with pumping intensity (Figure 38). It is obvious that, for a case that is not responsible for x-ray lasing, gain is directly proportional to intensity of the laser.

Using above two-pulse configuration does not rise the possibility of x-ray lasing considerably. The intensity is still needs to be improved; the improvement comes with the chirped pulse amplification (CPA) system. Pulse durations, intensities for both pulses and time delay between them are significant. Following figure (Figure 40), gives an example on an unsuccessful pumping configuration with pulse intensities of 1.5×10^{16} W/cm^2, 1.0×10^{19} W/cm^2 and pulse widths 200 ps, 50 fs for prepulse and main pulse, respectively. Time delay between them is kept 250 ps. This system does not work again. The configuration should be chosen carefully, usage of the code enables optimal preference.

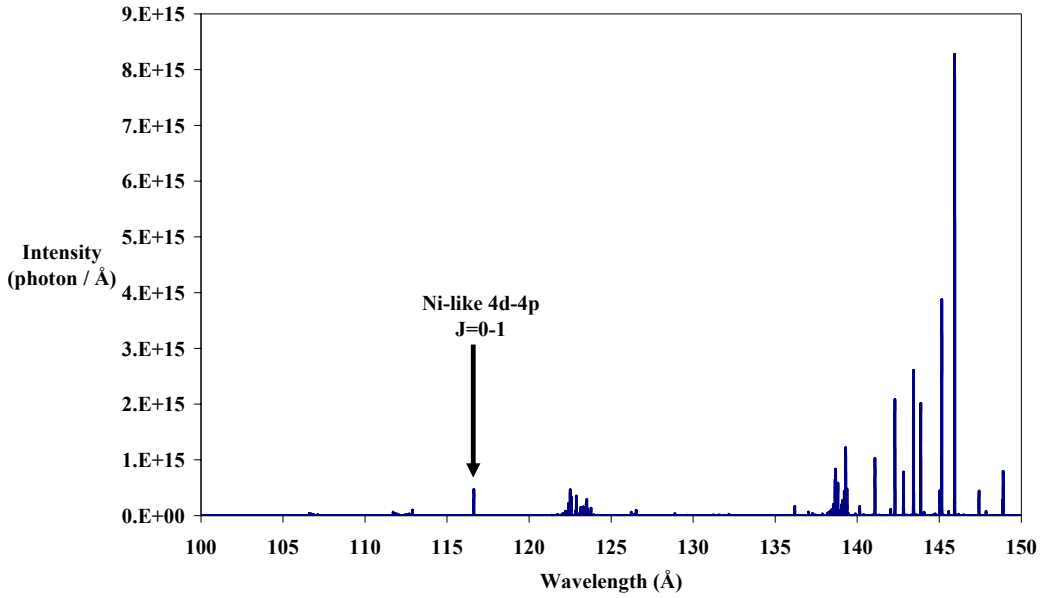

Figure 39 Two-pulse pumping with intensity of 5.42×10^{12} W/cm^2 and pulse duration of 6 ns

Another system with a successful arrangement of two pulses from CPA system can be analyzed and compared according to electrons removed, electron temperature and density. In the system by Kawachi et al., two same FWHM-pulses (4 ps) with different intensities ($1.5x10^9$ W/cm^2 and $1.0x10^{12}$ W/cm^2) irradiate the tin target from 1053 nm Nd:glass laser consists of a mode-locked Ti:sapphire oscillator [16]. Second pulse is activated after 1.2 ns the first gone. In Figure 41, with the usage of CPA technique therefore TCE scheme, more than 40 electrons can be removed from tin, which was around 20 for suggested QSS scheme experiment described above.

Electron temperature and density also have noticeable rise in the TCE scheme when compared to the classical QSS scheme. In the latter, electron temperature was 170 eV at most, however in the former, as seen in Figure 42, it is a few thousands of electron-volt.

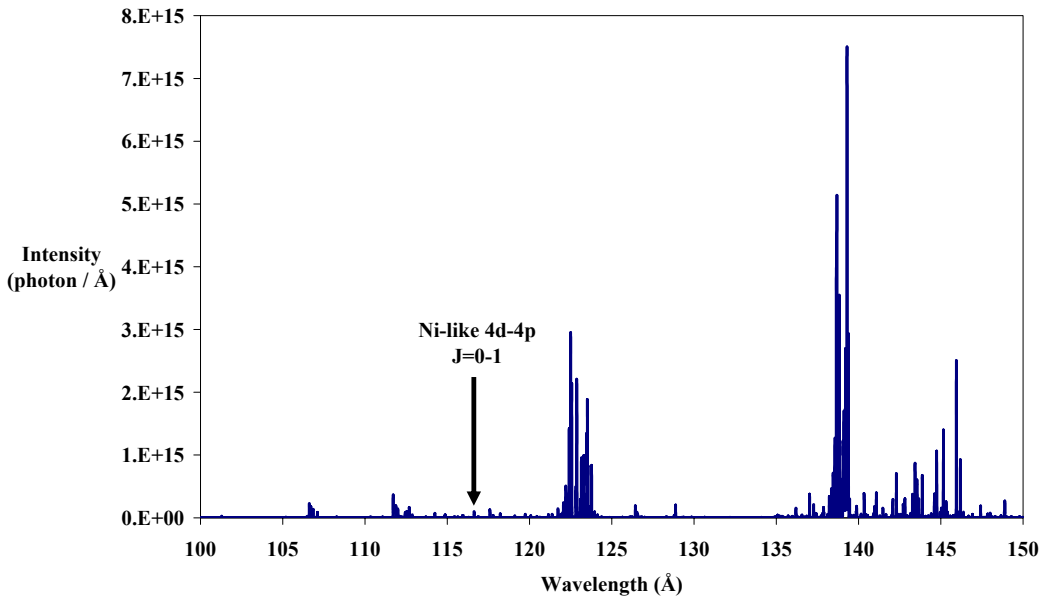

Figure 40 Two-pulse pumping

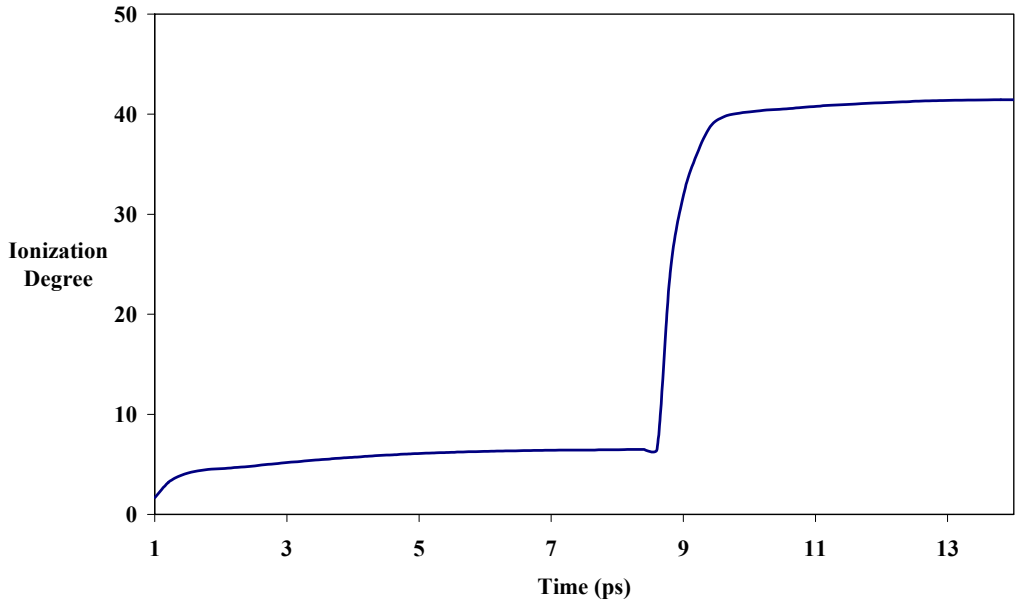

Figure 41 Ionization degree versus time graph for a two-pulse system with intensities 1.5×10^{9} W/cm^2 and 1.0×10^{12} W/cm^2

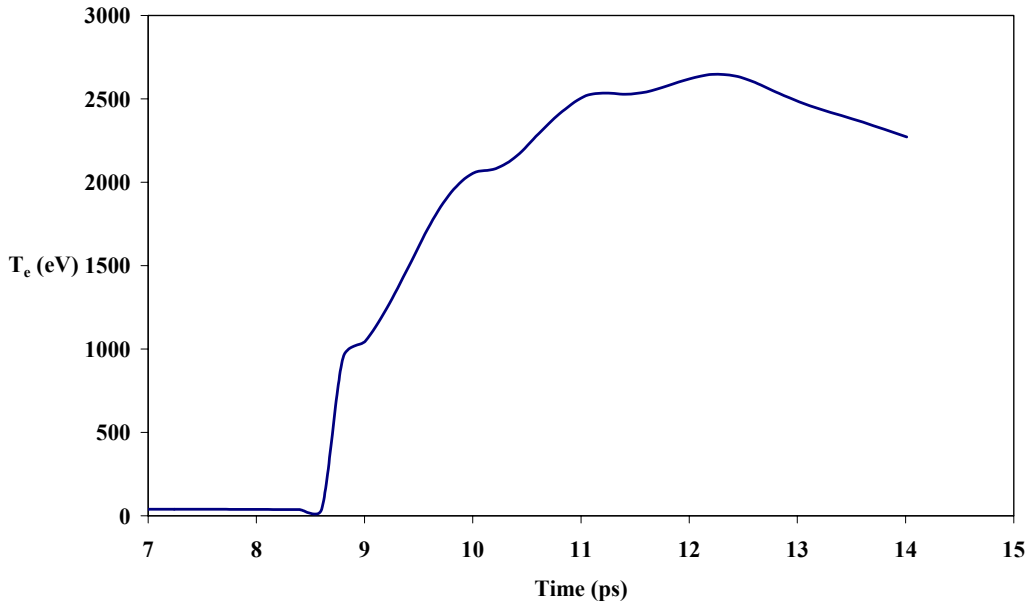

Figure 42 Electron temperature versus time graph for a two-pulse system with intensities 1.5×10^{9} W/cm^2 and 1.0×10^{12} W/cm^2

In the experiment with two 4 ps pulses with intensities $1.5x10^{9}$ W/cm^2 and $1.0x10^{12}$ W/cm^2, the electron density is 100 times more than that of the experiment with 6 ns-pulse at $4.00x10^{12}$ W/cm^2 (Figure 43).

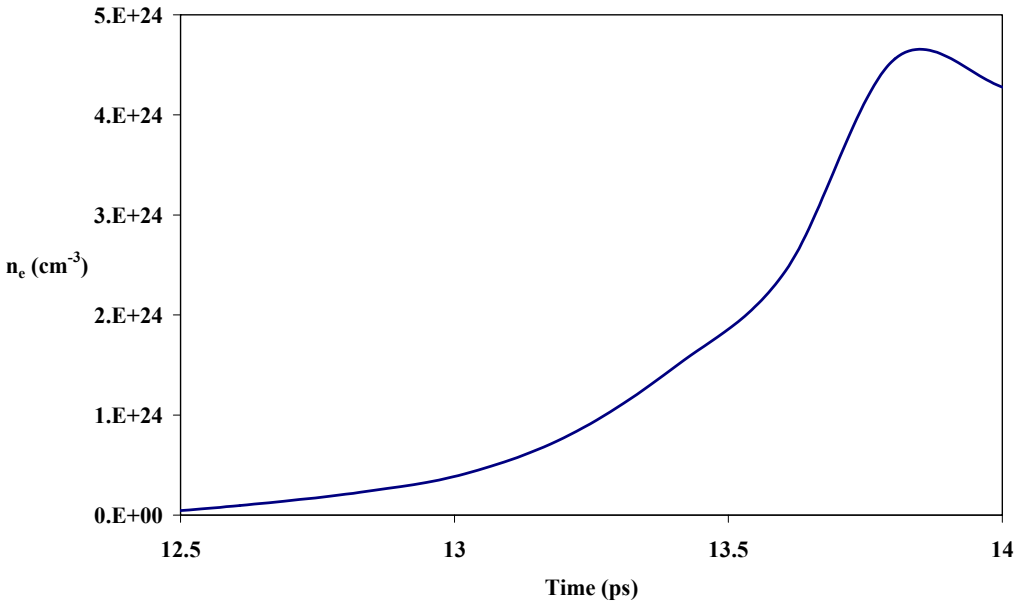

Figure 43 Electron density versus time graph for a two-pulse system with intensities $1.5x10^{9}$ W/cm^2 and $1.0x10^{12}$ W/cm^2

These higher values are sign for gain, indeed in the work of Kawachi and his co-workers. [16], the gain is calculated as ~30 cm^{-1} for 12 nm by the use of the HYADES 1D hydrodynamics code.

CHAPTER 5

SUMMARY AND CONCLUSION

In this study, x-ray regime is investigated mostly by the means of EHYBRID code which is the first step for constructing x-ray laser. With the help of the simulations optimum electron densities and temperatures are considered and the scheme that most fits to x-ray laser formation is underlined. The study can be evaluated as a preparation for construction of a CPA technique laser and encourages applications on x-ray laser.

X-ray formation is a new and exciting field because at this regime water becomes transparent and that facilitates the probing of living organisms. In order to create x-ray laser there are many possible ways; the preferable ones includes plasma media produced by a pumping laser. Among the two plasma-sourced schemes, laser produced plasma-based collisional x-ray lasers is more fertile than laser produced plasma-based recombination lasers. In the community it is concluded that collisional lasers are more effective than recombination lasers. On the other hand, OFI recombination lasers can be evaluated again with more efficient designs. Table-top lasers are practicable and give possibility to construct x-ray lasers compactly. In future, plasma based soft x-ray lasers with high harmonics can be tried to improve the usage.

Previously, QSS scheme, nanosecond pulse duration-lasers with intensities about 10^{11}-10^{12}. W/cm^2, were used to obtain x-ray regime radiation which is simulated in this work. The emission lines corresponding to x-ray regime are graphed. These emission lines showed that the possible lasing transition is not dominant, so the lasing for a high Z target, Sn, is not possible with pumping intensities on the order

of 10^{12} W/cm^2. Electron temperature, electron density and gain data obtained from the EHYBRID code also verifies the conclusion. This scheme can be improved with an intense and short pulse duration-laser usage. In that case, first heating and then ionizing the plasma in a short time interval (TCE scheme), lasing can exist. This new technique is considered again with the simulation code EHYBRID together with different studies including both experiments and simulation with different codes. EHYBRID output data showed that the electron temperature and density increased plentifully. As a conclusion, by the means of simulations, it is shown that, quasi-steady state scheme is much more suitable to obtain x-ray lasing than transient excitation scheme.

The simulations showed that nanosecond pulse duration-, low intensity-laser is an adequate tool to investigate x-ray regime. The next topic should be investigating the x-ray lasing and then executing the applications, especially lithography. For this purpose a CPA table-top laser is under construction in METU Physics laser laboratory.

Extreme ultraviolet lithography is a developing technology expected for the mass production of next generation integrated circuits. Laser produced plasma is an attractive light source for the EUV lithography in terms of its brightness and compactness. Laser produced tin plasma has a highly intense emission peak at 13.5 nm of wavelength, thus much effort is devoted to the development of the Sn-based EUV light source all around the world. Our country can compete with them after the realization of the laboratory.

X-ray laser construction, its applications together with the underlying science, addition of new physical concepts and improvement of the common system can be studied as the PhD thesis which is the next aim of the author, her supervisor and instructors.

REFERENCES

[1] Matthews D. L., Hagelstein P. L., Rosen M. D., B. J. MacGowan et. al., 1985, Phys. Rev. Lett., 54, 110-114

[2] Rosen M. D., Hagelstein P. L., Matthews D. L., B. J. MacGowan et. al., 1985, Phys. Rev. Lett., 54, 106-109

[3] Tallents G. T., 2003, J. Phys. D: Appl. Phys., 36, R259–R276

[4] Qi Wang Q., Yuanli Cheng Y., Yongpeng Zhao Y., 2002

[5] Moreno C. H., Marconi M. C., Shlyaptsev V. N., Benware B. R., Macchietto C. D., Chilla J. L. A., Rocca J. J., Osterheld A. L., 1998, Phys. Rev. A, 58, 1509-1514

[6] Biedron S. G., Bartolini R., Ciocci F., Giuseppe Dattoli G., et al.,2002, LASE 2002 High-Power Lasers and Applications Directed Energy Laser and Beam Control Technologies

[7] Chou M.-C., Chu H.-H., Tsai H.-E., Lin P.-H., Yang L.-S., Chen D.-L., Lee C.-H., Lin J.-Y., Wang J., Chen S.-Y., 2005, Optics & Photonics on Soft X-Ray Lasers and Applications VI, San Diego, California, USA

[8] Sebban S., Mocek T., Ros D., Upcraft L., Balcou Ph., Haroutunian R., Grillon G., Rus B.,. Klisnick A, Carillon A., Jamelot G., Valentin C., Rousse A., Rousseau J. P., Notebaert L., Pittman M., Hulin D., 2002, Phys. Rev. Lett., 89, 253901-1-253901-4

[9] High-Field Physics and Ultrafast Technology Laboratory High-Field Physics and Ultrafast Technology Laboratory, High-Field Physics and Ultrafast Technology Laboratory, http://ltl.iams.sinica.edu.tw/, July 2006

[10] Zhang J., Key M. H., Rose S. J., Tallents G. J., 1994, Phys. Rev. A,49, 4024-4030

[11] Carillon A., Chen H. Z., Dhez P., Dwivedi L., Jacoby J., Jaegle P., Jamelot G., Key M. H., Kidd A., Klisnick A., Kodama R., Krishnan J., Lewis C. L. S., Neely D., Norreys P., O'Neill D., Pert G. J., Ramsden S. A., Raucort J. P., Tallents G. J., Uhomoibhi J., 1992, Phys. Rev. Lett., 68, 1917-1920

[12] Nilsen J., Bajt S., Chapman H. N., Staub F., Balmer J., 2003, Opt. Lett., 28, 2249-2251

[13] Smith R. F., Dunn J., Nilsen J., Shlyaptsev V. N., Moon S., Filevich J., Rocca J. J., Marconi M. C., Hunter J. R., and Barbee Jr. T. W., 2002. Phys. Rev. Lett., 89, 065004-1-065004-4

[14] Tallents G. J., Abou-Ali Y., Demir A., Dong Q., Edwards M. H., Mistry P., Pert G. J., 2004, IEEE, 10, 1373

[15] Dunn J., Osterheld A. L., Shepherd R., White W. E., Shlyaptsev V. N., Stewart R. E., 1998, Phys. Rev. Lett., 80, 2825-1828

[16] Kawachi T., Kado M., Tanaka M., Sasaki A., N Hasegawa N., Kilpio A. V., Namba S., Nagashima K., Lu P., Takahashi K., Tang H., Tai R., Kishimoto M., Koike M., Daido H., Kato Y.,2002, Phys. Rev. A, 66, 033815-1-033815-7

[17] MacPhee A. G., Lewis C. L. S., O'Rourke R. M. N., Lin J. Y., Demir A., Tallents G. J., Neely D., Ros D., Zeitoun Ph., McCabe S. P., Pert G. J., Simms P.,

1997/98, CLF Annual Report, Science – High Power Laser Programme – Short Pulse Plasma Physics, 44-45

[18] Dendy R., 1993, Plasma Physics An Introductory Course, Cambridge University Press, 323-324

[19] Chen F. F., 1983, Plasma Physics and Controlled Fusion, Plenum Press

[20] Wikimedia Foundation, Inc., Plasma (physics), http://en.wikipedia.org/wiki/Plasma_(physics),26 August 2006

[21] Kuba J. PhD Thesis: Experimental and Theoretical Study of X-ray Lasers Pumped by an Ultra-Short Laser Pulse: Transient Pumping of Ni-like Ag Ions, 2001, Czech Technical University in Prague

[22] McCabe S., Pert G. J., 2000, Phys. Rev. A., 61, 033804-1-033804-9

[23] Holden P. B., Healy S. B., Lightbody M. T. M., Pew G. J., J A Plowes, A. E. Kingston., Robertson E., Lewis C. L. S., Neelys D., 1994, J. Phys. B: At. Mol. Opt Phys., 27, 341-367

[24] Demir A., Kenar N., Tallents G. J., 2004, Appl. Phys. B, 78, 945–948

[25] Turcu I. C. E et al., 1994, SPIE Proc. 2015, 243-260

[26] Wikimedia Foundation, Inc., http://en.wikipedia.org/wiki/Extreme_ultraviolet_lithography, Extreme ultraviolet lithography, 26 August 2006

[27] Harilal S. S., O'Shay B., Tillack M. S., Tao Y., Paguio R., Nikroo A., Back C. A., 2006, J. Phys. D: Appl. Phys. 39, 484

[28] Spitzer R. C., Kauffman R. L., Orzechowski T., Phillion W., Cerjan C., 1993, J. Vac. Sci. Technol. B, 11, 2986-2989

[29] Harilal S. S., O'Shay B., Tillack M. S., Tao Y., Paguio R., Nikroo A., Back C. A., 2006, J. Phys. D: Appl. Phys., 39,484-487

[30] Shimada Y., Nishimura H., Nakai M., Hashimoto K., Yamaura M. Et al., 2005, Appl. Phys. Lett., 86, 051501

[31] Kieft E. R., Garloff K., van der Mullen J. J. A. M. , Banine V.

[32] Harilal S. S., O'Shay B., Tao Y., Tillack M. S., 2006, J. Appl. Phys., 99, 083303-1-083303-10

[33] Da Silva L. B., London R. A., MacGowan B. J., Mrowka S., Matthews D. L., Craxton R. S., 1994, Opt. Lett. 19, 1532-1534

[34] L. Yuelin, P. Georg, L. Peixiang,E. F. Ernst, 1995, Phys . Rev. A, 53, 652

[35] Healy S. B., Cairns G. F., Lewis C. L. S., Pert G. J., Plowes J. A., 2000, Phys. Rev. A, 1, 949-957

[36] Milchberg H. M., McNaught S. J., Para E., 2001, Phys. Rev. E, 64, 056402-1- 056402-7

[37] Kaçar E., PhD Thesis: Ne- ve F- Benzeri İyonlardan Yayılan Rezonans Çizgi Spektrumlarının Hesaplanması, 2004, Kocaeli Üniversitesi

[38] Lu X., Li Y., Zhang J., 202, Phys. Plas. 9, 1412-1415

[39] Simms P. A., McCabe S., Pert G. J., 1998, Opt. Commun., 153, 164-171

[40] Smith R. F., Benredjem D., et. al., 2002, preprint, U.S. Department of Energy, LLNL

[41] Department of Chemical Engineering at the University of Patras, Plasma Technology Laboratory, http://www.tfd.chalmers.se/~md8hemra/modeling.htm, 27 August 2006

[42] V.A.Lisovsky and V.D.Yegorenkov,1994, Plasma Science, Conference Record - Abstracts., 1994 IEEE International Conference

[43] Demir A., Lecture Notes, METU, 2006

[44] The Department of Applied Mechanics, Mechanical Engineering research at Chalmers, Chalmers, http://www.tfd.chalmers.se/~md8hemra/modeling.htm, July 2006

[45] Natural Defense National Association, Minisi M. D., Gelatin Impact Modeling, http://www.dtic.mil/ndia/2006smallarms/minisi.pdf, 1 January 2005

[46] Hill NE Exhibit Hall, Albuquerque Convention Center, A Collisional Radiative Code for Plasma Modeling, http://flux.aps.org/meetings/YR02/APR02/baps/abs/S200075.html, August 2006

[47] Soukhanovskii V.A., Lippmann S., May M.J., Finkenthal M., Moos H.W., Fournier K.B., Goldstein W., Pacella D., Mazzitelli G., 1999, Astron. Astrophys. Suppl. Ser. 142, 95-106

[48] Pert G. J., 1983, J. Fluid Mech., 131, 401

[49] Abou-Ali Y., Demir A., Tallents G.J., Edwards M., King R. E., Pert G. J., 2003, J. Phys. B: At. Mol. Opt. Phys., 36, 4097–4106

[50] Holden P. B., Pertz G. J., 1996, J. Phys. B: At. Mol. Opt Phys., 29, 2151-2157

[51] Cowan R. D., 1981, The Theory of Atomic Structure and Spectra, The University of California Press